

Secondary Electron Emission from Thin Diamond Films

Sophie Osbourne

2014

Supervisor: Professor Paul May

Second Assessor: Dr Neil Fox

School of Chemistry

Physical and Theoretical Chemistry Section

A report submitted in partial fulfilment for the honours degree of MSci at the University of
Bristol



University of
BRISTOL

Abstract

Secondary electrons are emitted from the surface of a solid upon excitation by primary electrons, if they have a high enough energy to escape the surface into vacuum. Diamond surfaces are particularly well suited to secondary electron emission, and secondary electron yields of over 100 have been measured for diamond films. Secondary electron emission of diamond films has been measured in both reflection and transmission modes, although far fewer transmission mode experiments have been carried out. Samples for transmission mode must be much thinner, and the primary electron beam must be sufficiently high to generate electrons which can diffuse to, and consequently escape from, the other side of the diamond film.

Secondary electron emission experiments were carried out using a custom-built setup in the University of Bristol Diamond Laboratory; different configurations of screens within the setup were used to measure secondary electron emission for both reflection and transmission modes. Secondary electron emission has been measured for six undoped diamond films with thicknesses of 20 nm, 35 nm, 60 nm, 80 nm, 120 nm and 150 nm in both reflection and transmission modes. A secondary electron yield of 2.90 at a primary beam energy of 500 eV has been measured in reflection mode for the 20 nm sample, while a yield of 0.43 at 750 eV has been measured in transmission mode for the 150 nm sample.

Secondary electron emission can be modelled using Monte Carlo simulation, which is useful for predicting secondary electron yields and transmission energies but the software lacks the capability to distinguish between reflection and transmission modes when calculating secondary electron yields. A free-to-download simulation program called CASINO has been used to simulate secondary electron emission: the 2D version has been used to determine the primary beam energy at which primary electrons start to be transmitted through the diamond films, while the 3D version has been used to simulate the secondary electron yield curves for all six samples used in the experiments for several different work functions. While the simulations currently provide an estimate of the expected experimental results, further edits to the code would improve the capability of the program.

Contents

Abstract.....	1
1 Introduction	4
1.1 Diamond.....	4
1.1.1 Manufacturing Synthetic Diamond.....	5
1.1.2 CVD Diamond Films.....	8
1.2 Secondary Electron Emission	10
1.2.1 Secondary Electron Yield.....	13
1.3 Diamond Surfaces and Secondary Electron Emission.....	15
1.4 Models Describing Secondary Electron Emission	16
1.5 Secondary Electron Emission from Diamond: Examples from Literature.....	17
1.5.1 Reflection Studies	20
1.5.2 Transmission Studies.....	23
1.6 Aims of the Project.....	25
2 Experimental	25
2.1 Samples.....	25
2.2 Experimental Method	26
2.2.1 Reflection Measurements.....	31
2.2.2 Transmission Measurements.....	32
2.3 Modelling Secondary Electron Emission.....	32
2.3.1 Secondary Electron Emission Modelling Software	32
2.3.2 CASINO	35
3 Results and Discussion	38
3.1 Reflection Experiments.....	38
3.2 Transmission Experiments	40
3.2.1 Transmission Simulations.....	41
3.2.2 Phosphor Screen Experiments	43
3.2.3 Copper Screen Experiments.....	46

3.3	CASINO 3D Simulations.....	55
4	Conclusions	58
5	Future Work.....	59
6	Acknowledgements.....	63
7	References	64
8	Appendix	71
8.1	Glossary of Terms.....	71
8.2	CASINO 3D Simulation Plots.....	73

1 Introduction

1.1 Diamond

Diamond is a naturally occurring allotrope of carbon, where the carbon atoms are arranged in a tetrahedral structure. Each carbon atom is sp^3 hybridised and bonded to its four nearest neighbours¹. The diamond unit cell is a face-centred cubic (fcc) structure with two atoms in each primitive cell, shown in Figure 1.

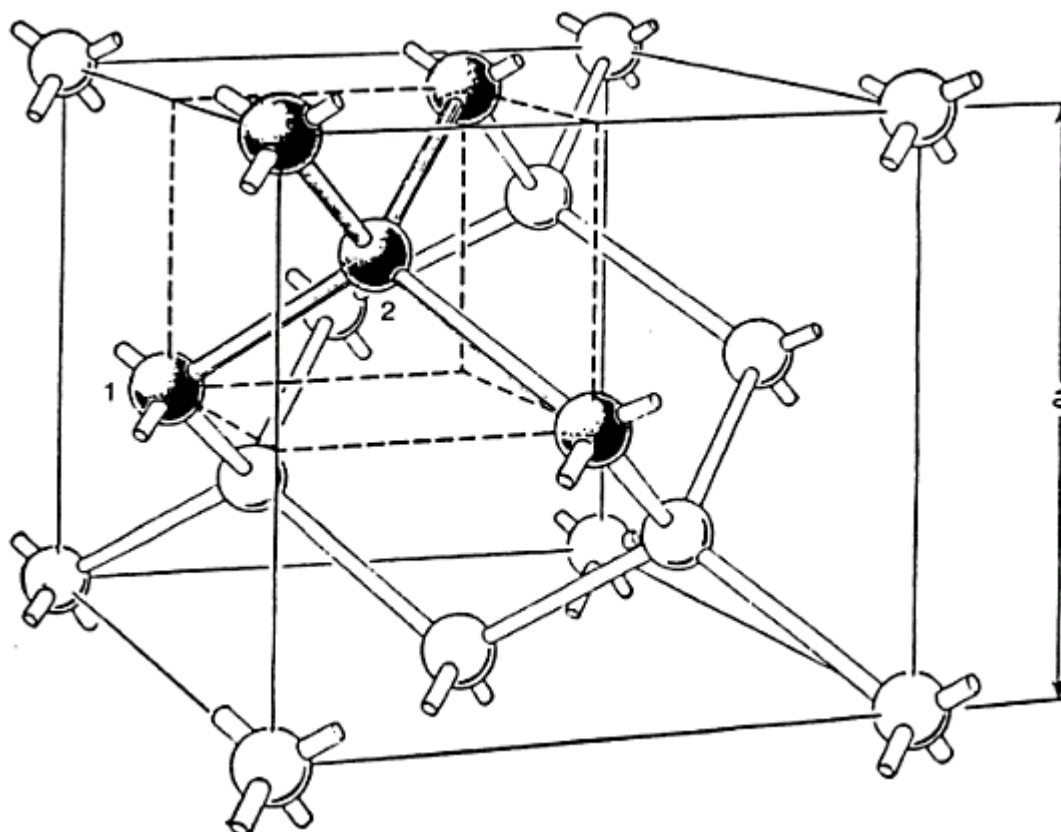


Figure 1: Diagram showing the tetrahedral arrangement of the diamond atoms within the unit cell. The diamond unit cell can be thought of as two interpenetrating fcc cells, with the numbers 1 and 2 in the diagram representing the two inequivalent carbon atoms of the smallest unit cell. The letter *a* represents the lattice constant of the cell, which for diamond is 3.567\AA^2 . Diagram reproduced from *Properties, Growth and Applications of Diamond (2001)*³.

The 'diamond structure' is the same covalently bonded structure adopted by other group IV elements in bulk: namely silicon and germanium². However, diamond possesses a number of unique properties compared to silicon and germanium, such as a large bulk modulus and small lattice constant⁴. The properties of diamond are often extreme, and it is a combination of the properties given in Table 1, along with its resistance to chemical corrosion and high radiation hardness, that

make diamond such a desirable material for a large range of applications such as its possible use as a potential biochip or biomarker⁵, or in vacuum electronics for gated cathodes and other photoemission devices⁶.

Property	Value	Units
Bandgap	5.45	eV
Bulk Modulus	1.2×10^{12}	N m^{-2}
Compressibility	8.3×10^{-13}	$\text{m}^{-2} \text{N}^{-1}$
Density	3.52	G cm^{-3}
Electron Mobility	2200	$\text{cm}^2 \text{V}^{-1} \text{s}^{-1}$
Mechanical Hardness	90	GPa
Resistivity	10^{16}	$\Omega \text{ cm}$
Thermal Conductivity	2×10^3	$\text{W m}^{-1} \text{K}^{-1}$
Thermal Expansion Coefficient	0.8×10^{-6}	K^{-1}
Young's Modulus	1.22	GPa

Table 1: Table documenting some of the properties of diamond which makes it unique, given at room temperature unless otherwise stated. Table adapted from Ashfold et al.'s 1994 review⁷ and *Synthetic Diamond: Emerging CVD Science and Technology (1994)*⁸.

Due to diamond's many outstanding properties, it is often investigated as a potential material for a range of devices, from optical to electronic. For these purposes, synthetic diamond films are often manufactured as control of dopants and surface characteristics can provide films tailored for a specific purpose.

1.1.1 Manufacturing Synthetic Diamond

In order to overcome the large activation pressure to convert graphite to diamond, a high pressure, high temperature (HPHT) method was developed, which mimics the conditions under which diamond is formed naturally⁹. In the HPHT method, graphite and a catalyst are subjected to pressures of around 55000 atm and temperatures of 2000°C ¹⁰. Usually the catalyst is a transition metal alloy such as cobalt, nickel or iron alloys, but carbonates of lithium, sodium and magnesium have been used successfully under similar reaction conditions¹¹. However, the single crystals grown using HPHT methods have limited uses in scientific and engineering applications, and the addition of dopants to favourably alter the electronic properties of the diamond grown was found to extend only to synthesis of p-type diamond with boron by Caveney¹². Another method, known as Chemical Vapour Deposition (CVD), was consequently developed to produce diamond films for a large range of applications.

CVD diamond films are manufactured via the use of a series of gas phase reactions of carbon containing gases above a substrate onto which individual carbon atoms can be deposited. The reactions in the gas phase, which tends to be composed of a mixture of CH_4 , H_2 , and gases containing the required dopant atoms, can be activated by a number of methods: hot filament, combustion flame, radio frequency, microwave-plasma and direct current activation methods have all been used, each requiring different reactant gases for optimal growth conditions¹³. Hot filament (HF) CVD is one of the most often used CVD techniques; it was the first CVD technique to produce continuous diamond films onto a substrate¹⁴. An example diagram of an HF CVD reactor is given in Figure 2; the setup was used by Chu et al. to investigate the mechanism of film growth via CVD for mixed ^{12}C and ^{13}C gases¹⁵.

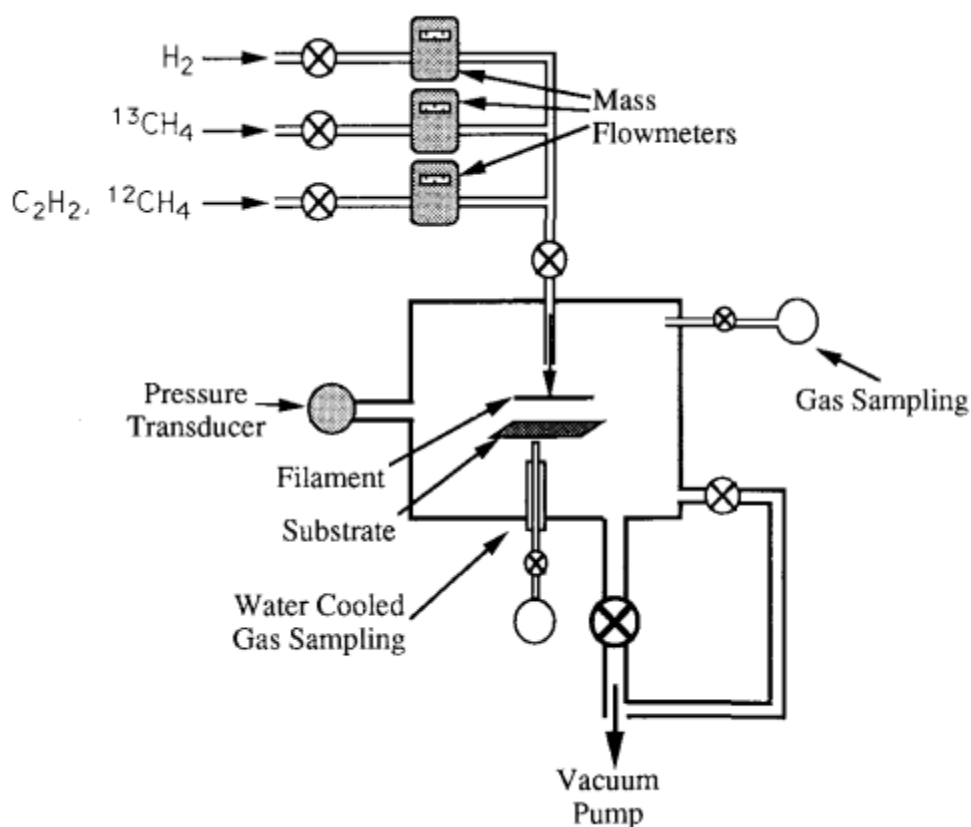


Figure 2: Diagram of a HF reactor, as used by Chu et al. in their 1990 research into mixed ^{12}C and ^{13}C film growth mechanism. The setup is typical of a HF reactor: the substrate is kept beneath the tungsten filament wires in a chamber kept at vacuum by a rotary pump. Mixtures of gases are pumped into the chamber, controlled by flowmeters. The reactor shown here operated at pressures of 24-27 Torr, substrate temperatures of 800-950°C and filament temperatures of 2000-2100°C. Methane ratios of 0.3-1.0% were used. Diagram reproduced from Chu et al.'s 1990 paper¹⁵.

Figure 2 shows a diagram of the HF reactor. The conditions for the $^{12}\text{C}/^{13}\text{C}$ experiment are typical of HF reactor conditions: these reactors usually operate at pressures of between 20 Torr and 30 Torr, with a substrate temperature in the range 600-1200°C and a filament temperature between 2000°C and 2600°C^{16,17,18}. The gas phase is usually made up of around 1% CH_4 diluted in H_2 , although N_2 can be included in small amounts (between 5% and 10% of the total gas volume in the chamber) to increase the growth rate of the film: at high temperature filaments (around 2500°C) higher additions of N_2 increased film growth rate, while for lower temperature filaments (around 2200°C) smaller amounts of N_2 increased the growth rate¹⁹.

CVD diamond growth is due to a complex series of reactions which take place within the precursor gases once they have passed over the activation site – in an HF reactor, the activation would be provided by the tungsten hot filament. As the molecules pass over the filament, causing the gases to heat to 2000°C or higher, the molecules fragment to form reactive radicals, such as $\cdot\text{CH}_3$, as well as C and H atoms. These fragments continue past the filament towards the substrate via diffusion and convection, continuing to react with each other while in the gas phase²⁰. Eventually the fragments reach the substrate, and can either adsorb to the surface or desorb back into the gas phase. Fragments may also diffuse along the substrate to find a reaction site: $\cdot\text{CH}_3$ radicals will diffuse along the substrate surface to find a monoradical site, although $\cdot\text{CH}_3$ have been found to bind to biradical sites²¹. While the steps described here give a very basic overview of CVD reactions, the final addition of the $\cdot\text{CH}_3$ radicals to the substrate is the driving step in diamond growth. A simplified diagram showing the flow of precursor gases over the activation site, leading to fragments which eventually adsorb onto the substrate surface, can be seen in Figure 3.

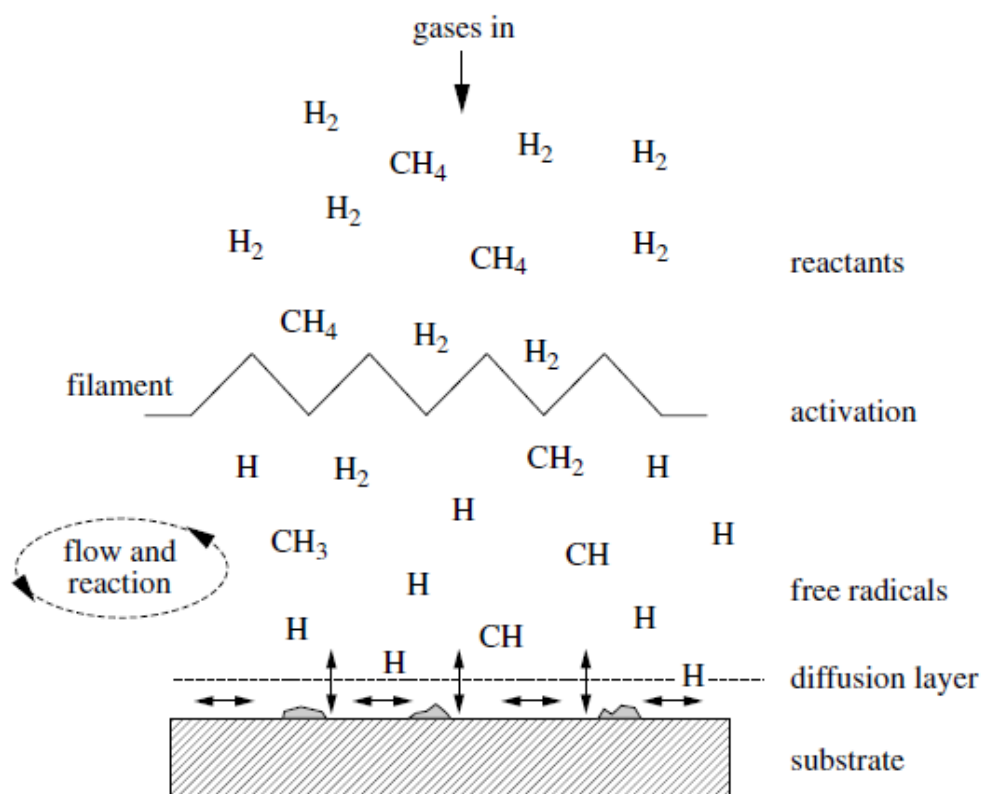


Figure 3: Schematic showing the processes within an HF reactor for growing CVD diamond films. The same principle of precursor gases passing over an activation site to form free radicals before adsorption to the surface applies to all CVD techniques. Diagram reproduced from May's 2000 review¹⁸.

1.1.2 CVD Diamond Films

Growth of diamond via CVD allows control of the type of diamond grown. Different film qualities, such as single crystal, microcrystalline or nanocrystalline, give different surface morphologies, while doping with atoms such as boron or nitrogen allow the electrical properties of the film to be altered.

Diamond films can be classified according to their morphology, as either single crystal films or polycrystalline films. Polycrystalline diamond films include microcrystalline, nanocrystalline and ultrananocrystalline, however compared to single crystal films these films can have a large number of structural defects due to the grain boundaries between the individual crystals. Single crystal films are therefore more desirable for electrical applications as current is not blocked by grain boundaries as in polycrystalline films²².

The three types of polycrystalline films are a result of slightly different growth conditions and methane ratios in the precursor gases. Microcrystalline films are usually grown in methane/hydrogen ratios of 2%, while for nanocrystalline films the ratio is slightly higher at 3% or

more. Ultrananocrystalline diamond is grown in reactors containing a majority of argon rather than hydrogen as one of the precursor gases, with comparatively small amounts of hydrogen²³. The different growth conditions of the films result in different grain sizes and sp^2 content of the films: microcrystalline films have the largest grains and the smallest sp^2 content, while ultrananocrystalline films have the smallest grains and largest sp^2 content¹⁷. An example of the different growth conditions of the film types is given in Table 2.

	Microcrystalline	Nanocrystalline	Ultrananocrystalline
Pressure / kPa	0.9-2.0	2.7-4.4	16.0
Power / W	700	700	1200
Temperature / °C	450-550	625-725	<650
Time / h	40	5-20	5-6
H₂ Flow / sccm	200	200	1-2
CH₄ Flow / sccm	3	3	1
CO₂ Flow / sccm	8	8	0
Ar Flow / sccm	0	0	100
Grain size / nm	5000-10000	20-50	3-5

Table 2: Table detailing the different growth conditions for polycrystalline diamond films and the resulting grain sizes of the crystal. Table adapted from Reinhard's 2004 paper²⁴, with additional information on grain sizes from *Growth and Characterization of Nanocrystalline Diamond Films for Microelectronics and Microelectromechanical Systems (2008)*²⁵.

Single crystal diamonds can also be classified according to the defects within them: the classification system sorts them into Type Ia, Type Ib, Type IIa and Type IIb. Type I diamonds contain nitrogen – Type Ia has nitrogen on interstitial sites in the diamond lattice while diamond with nitrogen on substitutional lattice sites is Type Ib. Here nitrogen does not play a role as a dopant and Type I diamonds are insulators at room temperature due to the deep donor level formed in the diamond²⁶. Type IIa diamonds have no nitrogen impurities, while Type IIb is boron-doped and has semiconducting properties due to the electronically active impurities²⁷. Dopants can be incorporated into CVD films by the addition of gases containing the required dopant during growth, such as the addition of B₂H₆ as a precursor gas in order to grow boron-doped films²⁸.

One of the main advantages of CVD diamond growth techniques is the ability to tailor the thickness of the diamond films grown by varying the deposition time²⁹. Control of film thickness is essential, particularly for films used in secondary electron emission experiments where film thickness affects the yield measured³⁰.

1.2 Secondary Electron Emission

When a beam of primary electrons of sufficient energy is accelerated onto the surface of a solid, the electrons can interact with the sample in a number of different ways, resulting in the emission of secondary electrons³¹. Upon the interaction of the primary electrons with the solid, the electrons lose their energy as a result of several different types of interaction, such as elastic and inelastic scattering or x-ray generation³². A diagram showing the types of radiation and electrons emitted is shown in Figure 4, where the excitation volume (also known as the electron interaction volume) is the volume within a solid where the electron beam interacts with the sample³³; it is dependent upon the sample composition and the energy of the electron beam.

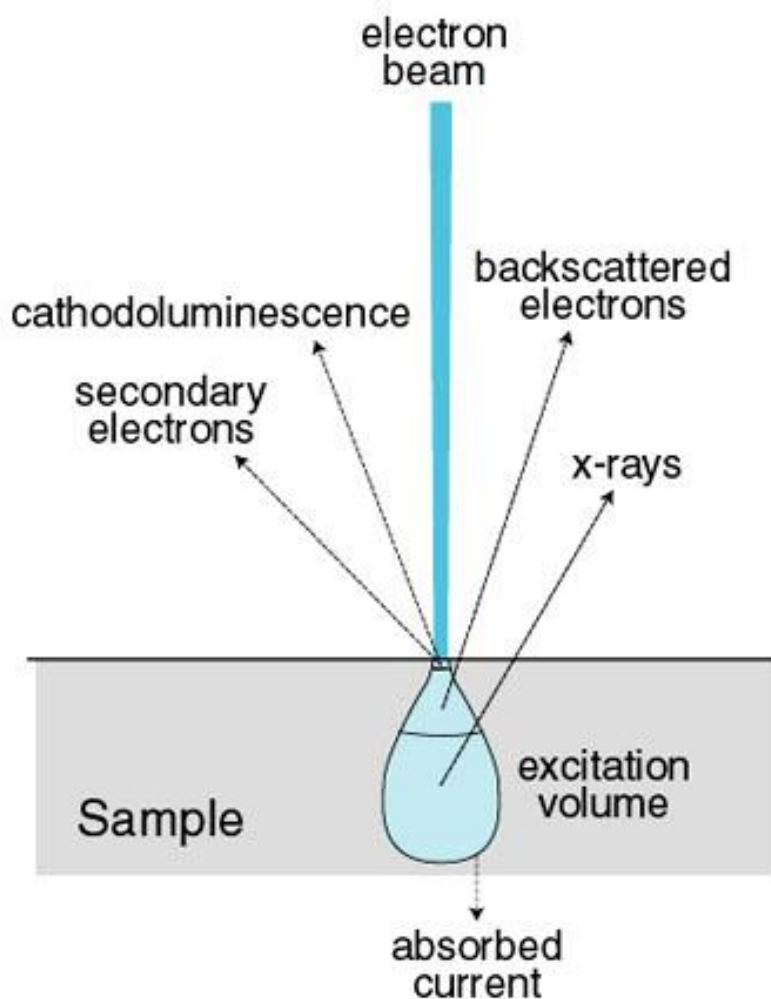


Figure 4: Diagram showing the incidence of an electron beam on a surface and the radiation and electrons that may be emitted as a result of electron interactions with the solid. Secondary electrons, backscattered electrons and radiation such as x-rays and cathodoluminescence (emitted visible light which is generated by incident electrons³⁴) can all be emitted from within the sample upon exposure to a primary electron beam. Diagram reproduced from the Northern Arizona University's Microanalysis Facility^o.

The secondary electrons can be classified according to their energies and their interactions within the solid. Backscattered electrons include elastically and inelastically scattered primary electrons³⁵: elastically scattered electrons are deflected through the sample at wide angles and suffer very little energy loss, and thus have energies close to that of the primary electron beam; inelastically scattered electrons have lost some of their kinetic energy upon interaction with the solid. Auger electrons are a type of backscattered electron, which result from the filling of an inner shell vacancy being accompanied by the emission of an electron (the Auger electron) from the same atom³⁶.

^a <http://www4.nau.edu/microanalysis/Microprobe-SEM/Signals.html>; accessed 09/04/2014

'True' secondary electrons are slow electrons, defined as those having an energy of under 50 eV in order to differentiate from other electrons being emitted from the surface of a sample³⁷. The 50 eV limit is an estimate, as there will be some secondary electrons emitted with energies higher than 50 eV, and some backscattered electrons will be emitted with energies less than 50 eV³⁸. However, both the number of high energy secondary electrons and low energy backscattered electrons is considered to be small; hence 50 eV is an accurate limit. Furthermore, the secondary electrons generated by excitation from the primary electrons can excite further secondary electrons in a cascade effect, if their energy is sufficient. A diagram of the spectrum of emitted electrons as a function of their energies can be seen in Figure 5.

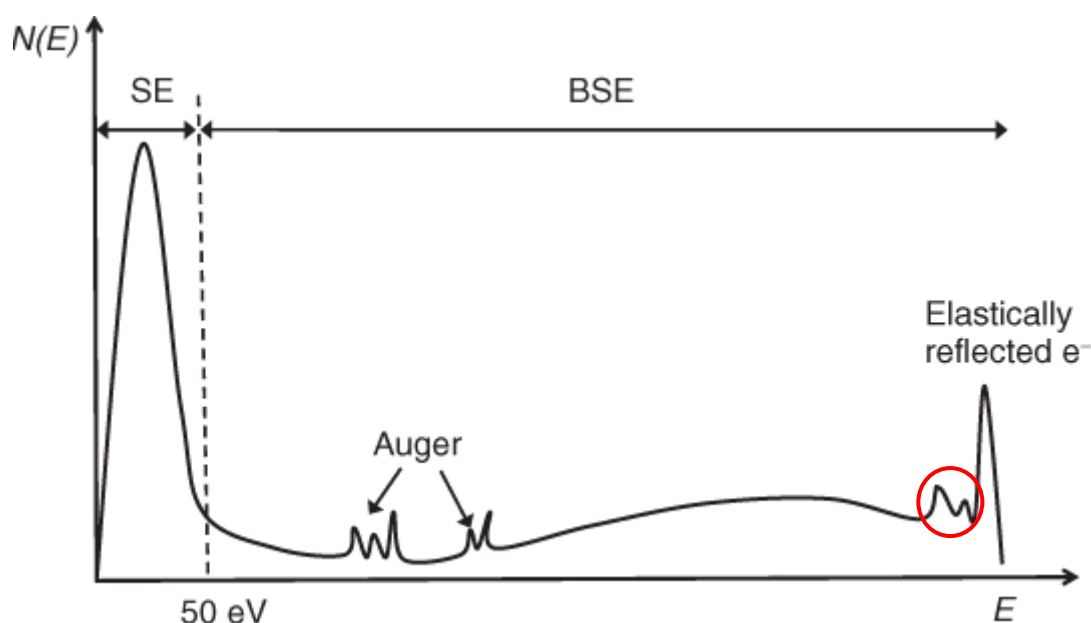


Figure 5: Schematic graph of the energy spectrum $N(E)$ (in arbitrary units) of emitted electrons from a surface after exposure to an incident beam. Secondary Electron (SE) and Back-Scattered Electron (BSE) regions are shown, as well as Auger electron peaks, peaks from elastically reflected electrons and peaks from inelastically scattered electrons (circled). Diagram edited from *Low Voltage Electron Microscopy: Principles and Applications*³⁹.

Figure 5 labels the types of electrons emitted from a sample as a function of their energy. The secondary electron curve below 50 eV is determined by the internal cascade process. The energy distribution of the secondary electron curve is independent of the incident electron beam energy⁴⁰. The backscattered electron region is made up of mostly inelastically scattered electrons; the elastically scattered electrons have lost a fraction of their energy during a single collision. The peaks in the backscattered region, such as those circled in Figure 5, are called 'characteristic losses'⁴¹.

The process of secondary electron emission is described as a three step process: the first step is the excitation of the secondary electrons in the solid by the primary electrons in the beam, second is the transport of the secondary electrons through the sample to the surface-vacuum interface, and the final step is the emission into the vacuum from the surface⁴². The transport of secondary electrons through the solid is through either a single-scattering event, or a diffusion process as a result of many scattering events. However, not all secondary electrons reach the surface of a sample, and of those, not all are emitted.

1.2.1 Secondary Electron Yield

The ratio of the total emitted electron current, I_t , to the primary electron current, I_0 , is known as the secondary electron yield⁴³ δ , given in Equation 1.

$$\delta = \frac{I_t}{I_0} \qquad \text{Equation 1}$$

In Equation 1, I_t includes all backscattered electrons as well as secondary electrons, and so δ more accurately describes the total yield. Secondary electron yield is often investigated as a function of the primary beam energy, which for most materials gives the same characteristic bell curve⁴⁴, as shown in Figure 6.

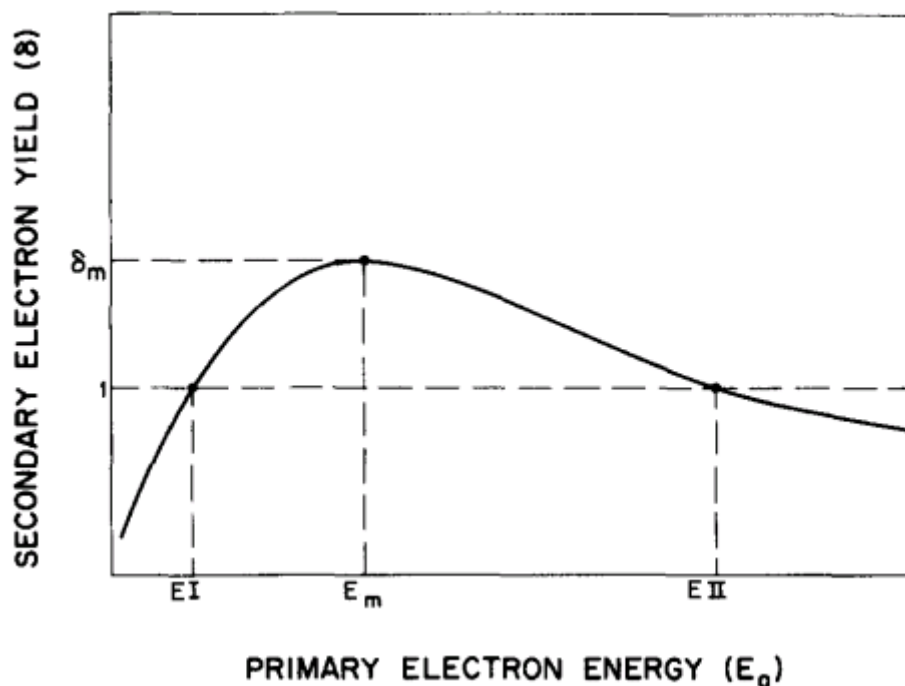


Figure 6: Schematic diagram of the secondary electron yield as a function of primary electron energy. The three characteristic parameters are indicated: E_I and E_{II} for which the yield is equal to one, and E_m for which the secondary electron yield is at a maximum, δ_m . Figure adapted from Dionne's 1975 paper⁴⁵.

Figure 6 shows an example secondary electron yield as a function of primary electron energy graph. E_I , E_{II} and E_m are known as the characteristic parameters; E_I and E_{II} indicate the energies at which the net current is zero, and therefore the number of incident electrons upon the surface of the sample is the same as the number of electrons emitted⁴⁶. The secondary electron yield graph can be explained in terms of the maximum penetration depth of the primary electrons and the escape depth of the secondary electrons⁴⁷. Below E_I , the primary electrons reflect back as their energy is not sufficient to penetrate the sample. The increase in yield between E_I and E_m is due to the much smaller penetration depth of the primary electrons compared to the escape depth of the secondary electrons, thus the secondary electrons escape and the secondary electron yield increases for primary electron beams with energies between E_I and E_m . The penetration and escape depths are equal when the secondary electron yield is at a maximum. The yield begins to decrease with primary electron beam energies above E_m as the penetration depth is now much greater than the escape depth, and so many of the generated secondaries are absorbed back into the sample before they can reach the surface.

1.3 Diamond Surfaces and Secondary Electron Emission

Diamond has many properties which make it a good candidate for secondary electron emission experiments. Diamond has a bandgap of 5.47 eV⁴⁸, where the bandgap is defined as the energy difference between the top of the valence band and the bottom of the conduction band (E_v and E_c respectively in Figure 7). The distribution of bands within a solid determine its conductivity: insulators have large bandgaps with filled valence bands and semiconductors small bandgaps, while metals have overlapping conduction and valence bands, and hence electrons are free to move throughout the solid. A diagram showing the band structure of diamond can be seen in Figure 7.

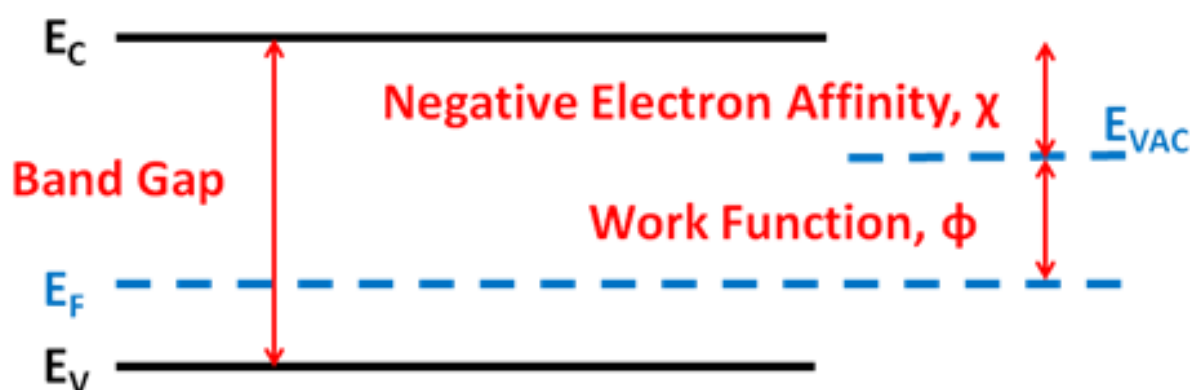


Figure 7: Diagram showing relative position of the different bands in diamond. E_c is the conduction band minimum, E_v is the valence band maximum, E_f is the Fermi level and E_{vac} is the vacuum level at which electrons can be emitted from the surface into the vacuum. The work function, ϕ , and the electron affinity, χ (which is negative for diamond), are also shown here.

When primary electrons strike the surface of diamond, secondary electrons are excited from the valence band into the conduction band and move to the surface of the solid. In diamond, the generated secondary electrons are able to escape the surface easily due to the negative electron affinity, χ , of the surface⁴⁹. The electron affinity of a material is the energy difference between the minimum of the conduction band and the vacuum level E_{vac} , with a material having either positive or negative electron affinities. A material has a positive electron affinity if the vacuum level lies above the conduction band minimum⁵⁰, while in materials such as diamond, the vacuum level lies below the conduction band minimum under certain conditions and diamond is therefore said to have a negative electron affinity⁵¹. Thus, when secondary electrons are generated by primary electrons and excited to the conduction band, they diffuse through the solid and upon reaching the surface are emitted as they do not encounter an energy barrier to overcome. The work function, ϕ , is the difference between the vacuum level and the Fermi level, E_f , defined as the maximum energy

an electron can have when it is at 0 K, or the energy level representing the probability that the occupation of the particular level is ½ at temperatures above 0 K⁵².

1.4 Models Describing Secondary Electron Emission

Several models exist for the description of secondary electron emission, and these have been adapted and improved upon over the years. This section aims to give an overview of the most commonly used models for secondary electron emission, particularly for those models used in simulations.

In 1957, Lye & Dekker developed a power-law theory for secondary electron generation in solids, and further added to their theory by including the effect of straggling primary electrons⁵³. Electron straggling is caused by a loss of energy via radiation and collisions⁵⁴, and including straggling in their calculations led to energy losses being equalised across the entire range of electron energies. Their analytical approach yielded Equation 2.

$$\frac{\delta}{\delta_m} = \frac{1}{g_n(z_m)} g_n\left(\frac{z_m E_0}{E_m}\right) \quad \text{Equation 2}$$

In Equation 2, z_m is the value of z needed to maximise the function $g_n(z)$, given by Equation 3.

$$g_n(z) = \frac{1 - e^{-z^{1.35}}}{z^{0.35}} \quad \text{Equation 3}$$

Vaughan reduced the formula given by Lye & Dekker to simplify it, so that the formula itself was written in fewer terms. He found that using their equation to work out secondary electron yields as a function of impact energy E_i gave close matches to those worked out using Equation 2⁴⁶. Vaughan's equation is given in Equation 4, with the ν function given in Equation 5.

$$\frac{\delta}{\delta_m} = (\nu - e^{1-\nu})^k \quad \text{Equation 4}$$

$$\nu = \frac{E_i - E_0}{E_m - E_0} \quad \text{Equation 5}$$

k is a parameter based on the value of ν given by Equation 5: if ν is greater than 1, then k is 0.25, while if ν is less than 1, then k is 0.62.

A generalised version of the relation dependent entirely on the energies of the primary electron beam was given by Lin & Joy in 2005, known as the semiempirical universal law for secondary electron emission. They used the law for Monte Carlo simulation of the secondary electron yields of 44 elements to compare to a database⁵⁵, and the model given by Lin & Joy is often built-in to

secondary electron simulation programs such as CASINO⁵⁶ (see section 2.3.2). The semiempirical universal law is given in Equation 6.

$$\frac{\delta}{\delta_m} = 1.28 \left(\frac{E_0}{E_m} \right)^{-0.67} \left[1 - e^{-1.614 \left(\frac{E_0}{E_m} \right)^{-0.67}} \right] \quad \text{Equation 6}$$

1.5 Secondary Electron Emission from Diamond: Examples from Literature

Secondary electron emission from diamond surfaces have been studied using both experimental techniques and simulations.

Many experiments carried out in the literature make use of a Faraday cup setup. A Faraday cup is a metal cup which, in secondary electron emission studies, encloses the sample under a high vacuum, with a small opening in the top to allow the primary electron beam to be aimed at the sample⁵⁷. Backscattered and secondary electrons are collected by the Faraday cup, generating a current if the Faraday cup is incorporated into a circuit⁵⁸. The current generated when the electrons are incident on the Faraday cup is I_t and hence the secondary electron yield can be calculated as the primary electron beam current is already known. However, it should be noted that a Faraday cup will collect all backscattered electrons: both those from elastic and inelastic collisions and true secondary electrons, as there is no experiment capable of distinguish the electrons according to their energy¹⁷.

Simulations of secondary electron emission are often based on Monte Carlo methods. The Monte Carlo method is a probabilistic based algorithm which uses repeated sampling to generate numerical data. Distributions of data can be generated by running the simulation continuously. For secondary electron emission, the electron trajectory is mapped using random numbers to determine the path length of the electron through the solid and the outcomes of scattering events⁵⁹.

Both reflection and transmission studies of secondary electron emission from diamond have been studied (see Figure 8). In reflection mode, the secondary electrons are emitted from the surface of the sample upon incidence of a primary electron beam. In transmission mode, a high energy electron beam is aimed at the surface of a thin sample, and secondary electrons are emitted from the other side.

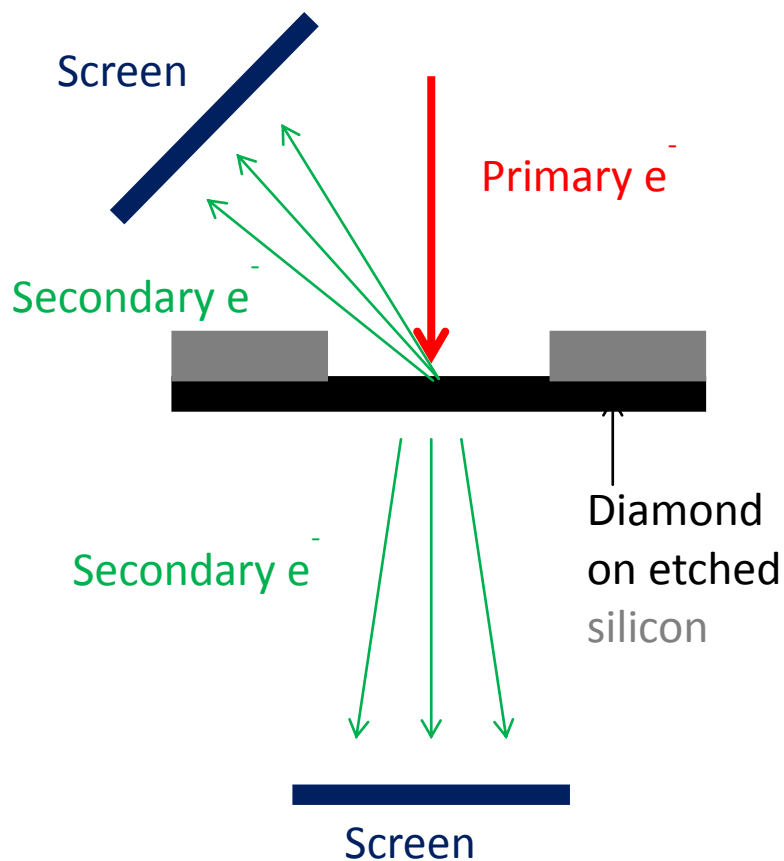


Figure 8: Diagram showing the difference between reflection and transmission measurements. In reflection mode, secondary electrons are emitted from the top surface of the sample at an angle and are collected by the upper screen in the diagram. In transmission mode, secondary electrons diffuse through the sample and are emitted from the bottom surface of the sample, here being collected by the lower screen.

Secondary electron yields from reflection modes tend to yield much higher values compared to those measured from transmission: secondary electron yields of 132 have been measured for diamond in reflection mode⁶⁰, compared to yields of 4 in transmission mode experiments⁶¹.

Yater et al. used secondary electron emission measurements on 8.3 μm diamond films to investigate the current amplification gains of single crystal diamond. The energy distribution curves for the maximum gains in both reflection and transmission mode are shown in Figure 9.

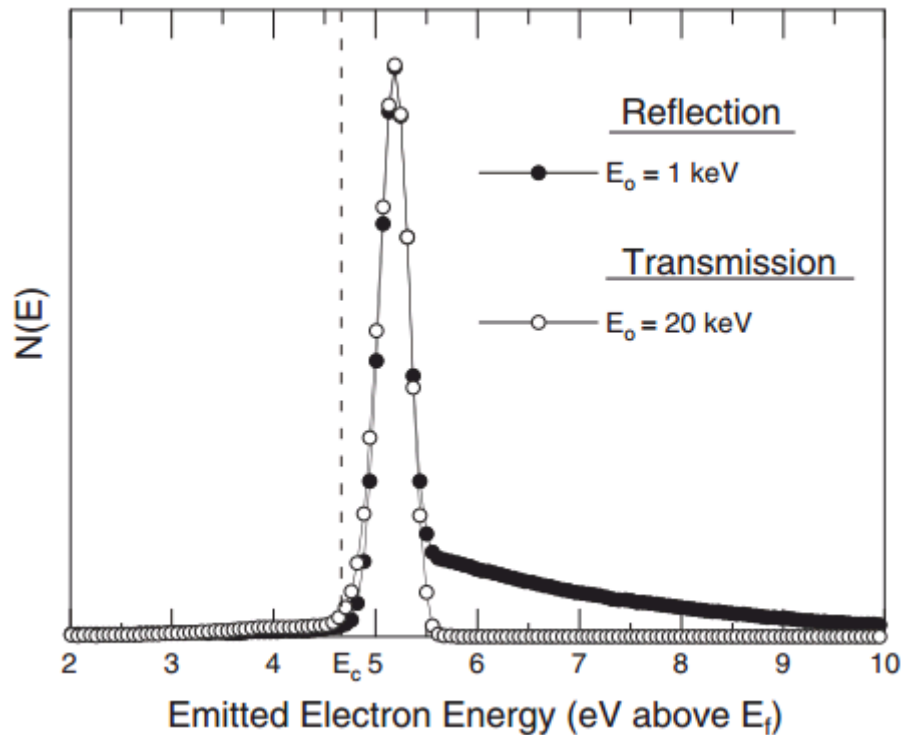


Figure 9: Normalised electron distribution curves for an 8.3 μm diamond film, where secondary electron measurements have been made in both reflection and transmission modes. The peak positions and peak width at FWHM for the two different modes are identical. Graph reproduced from Yater et al's 2011 paper⁶².

The normalised energy distribution curves shown in Figure 9 are very similar for both reflection and transmission measurements, with the peak of the curve at 0.54 eV above the dashed line E_c , and FWHM peak width measurements of 0.35 eV. However, the transmission mode measurements were made at substantially higher primary beam energies of 20 keV compared to 1 keV for reflection mode: the higher primary beam energies usually needed for transmission mode measurements is one of the main disadvantages of the setup. They measured a maximum secondary electron yield of 4 for transmission studies, and 18 for reflection studies.

Figure 10 shows a comparison between theoretical and measured secondary electron yields for an aluminium sample in a reflection setup, where the theoretical values were simulated using a particle-in-cell model rather than Monte Carlo simulation⁶³. For primary beam energies higher than 200 eV, the theoretical results lie within the error of the measured results. For beam energies less than 200 eV, the secondary electron yield for the experimental measurements are much higher than the simulation. The simulation only takes into account secondary electrons, however the nature of

the Faraday cup setup used for experimental results means that backscattered electrons from the primary beam are included in the measurements for secondary electron yield.

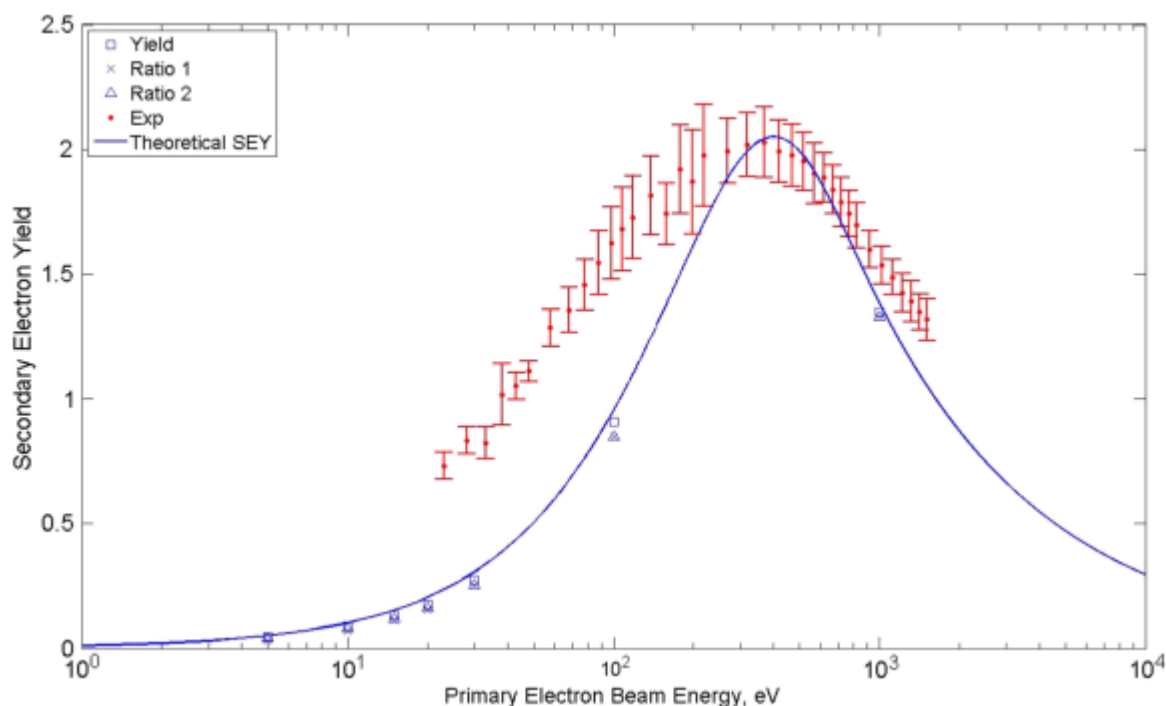


Figure 10: Comparison of simulated (blue line) and measured (red points) values for secondary electron yield as a function of primary beam energy for an aluminium sample. There is overall better agreement between yields at higher primary beam energy. Graph reproduced from Wang et al.'s 2012 paper⁶³.

While Figure 10 is not for a diamond sample, it shows that by choosing appropriate simulations there can be a fairly good match between measured and simulated results for secondary electron emission. The shape of the yield curves for both theoretical values and experimental measurements have an overall qualitative match, with the higher yields at lower primary electron beam energies for the experimental data are assumed to be due to backscattered electrons counting towards the yield rather than just secondary electrons, as the setup has no way of distinguishing between the two.

1.5.1 Reflection Studies

Secondary electron emission experiments are most often carried out in reflection mode, which is a far easier mode to measure secondary electron yield in. In reflection experiments, there is no need to grow fragile, thin free-standing films or to etch part of a substrate away in order to expose a diamond window. Manufacturing transmission mode samples is harder and the films can be liable to break when only nanometres thick. Consequently, as reflection mode experiments have been the focus of a majority of research, there is more literature available for reflection experiments. A small

selection of the data available will be reviewed here to give an idea of the many different experimental factors and differences between samples which can affect secondary electron yields.

Yater et al. have carried out several experiments on the secondary electron yield of diamond samples in reflection mode. Some of their experiments have focused on boron-doped samples with different surface morphology: single crystal, polycrystalline and nanocrystalline. All three samples were placed under an electron gun for secondary electron measurements using a Faraday cage^{61,64}. They found that the single crystal and polycrystalline diamond samples both had yields of 3, while the nanocrystalline sample had a higher yield of 16 when measured in reflection mode. Both sides of the nanocrystalline diamond were measured for a reflection yield as it had been removed from its substrate unlike the single crystal and polycrystalline samples, and the rear of the sample gave a lower reflection yield of 4, which the authors attributed to a poorer sample surface. Overall, the nanocrystalline diamond may have had a higher surface quality than both the other samples, as single crystal diamond has better electrical conductivity properties due to the lack of grain boundaries, and it would be expected to have a higher yield than polycrystalline diamond films.

Another factor which can affect the secondary electron yield of diamond samples is the surface termination. Surface termination describes the top layer of atoms on the diamond sample, where atoms other than carbon have bonded to the dangling bonds of the surface atoms. Termination removes any graphite formed on the surface from the dangling bonds recombining, which helps to give higher secondary electron yield as graphite is a poor secondary electron emitter³¹. Less electronegative species give higher secondary electron emission yields, with hydrogen and metals such as caesium giving higher yields than halogens such as fluorine⁶⁵. Yater et al. have compared the effect of surface termination on boron-doped, single crystal diamond samples with bare, hydrogen-terminated and caesium-terminated surfaces⁶⁶. The bare surface had a yield of 3 at a primary beam energy of 650 eV, while the hydrogen-terminated surface had a yield of 60 and the caesium-terminated surface had a yield of 132, at a higher primary beam energy of 2900 eV. The presence of hydrogen and caesium on the surface of the sample lowers the electron affinity to negative values, thus allowing low energy electrons to escape the vacuum barrier.

While for bare surfaces on boron-doped diamond, there was no discernible difference between the secondary electron yields measured on single crystal and polycrystalline diamond, the differences between single crystal and polycrystalline diamond yields are noticeable with different surface terminations. For boron-doped polycrystalline diamond samples, a hydrogen-terminated surface has a yield of 25, and a caesium-terminated has a yield of 77, again both at primary beam energies of 2900 eV. Polycrystalline diamond samples have grain boundaries which are not present in single

crystal samples; scattering of electrons by grain boundaries and other impurities, which could scatter escaping electrons back into the diamond sample, give single crystal samples and polycrystalline samples their different secondary electron emission characteristics.

The introduction of dopants to CVD grown films also has an effect on the secondary electron yield. Comparing polycrystalline, hydrogen-terminated samples, one doped with boron and one undoped, shows a secondary electron yield of 10 for the undoped sample⁶⁷, and a higher secondary electron yield of 84 for the boron-doped diamond⁴³. Shih et al.'s investigation into doping levels in polycrystalline diamond films found that up to a point, increasing the boron content could give yields as high as 84, and theorised that some boron is needed with the sample to provide electrical conductivity for the secondary electron process. However, too high a boron concentration leads to more frequent collisions of the secondary electrons with impurities within the diamond lattice, and the secondary electron yield decreases.

Undoped, hydrogen-terminated polycrystalline diamond has been grown on many different substrate types, including silicon (which is the substrate used in all experiments mentioned thus far in this section^{43, 61-67}), molybdenum, aluminium nitride, palladium and titanium. The secondary electron yields are given in Table 3, where the secondary electron yields range from 10-18 at room temperature. Secondary electron yields of over 45 have been measured for diamond on palladium substrates after heating to 700 K, while upon heating the diamond on titanium sample, no evidence of the film was found, suggesting inadequate adhesion of the film to the substrate⁶⁸. While at room temperature the substrate makes little difference to secondary electron yields, at higher temperature substrate choice can make a difference to the yield value.

	Substrate	Secondary Electron Yield
Ascarelli et al.	Si	10
Bekker et al.	Mo	12
Mearini et al.	AlN	15
	Pd	18
	Ti	13

Table 3: Table showing the differences in secondary electron yield of undoped, hydrogen-terminated polycrystalline diamond at room temperature. The secondary electron yield values were taken from Ascarelli et al.'s 2001 paper⁶⁷, Bekker et al.'s 1992 conference paper⁶⁹, and Mearini et al.'s 1994 paper⁶⁸.

1.5.2 Transmission Studies

A transmission configuration is preferable to a reflection configuration, as it avoids any adverse effects from the backscattered electrons passing the primary beam. However, the difficulty in manufacturing the micron thick films (or even less) means that only in the past ten years have transmission experiments on diamond films appeared in the literature.

Chang et al. did not simulate secondary electron emission; they measured the secondary electron yield of a 200 μm single crystal diamond sample at different primary beam energies, having measured no gain through a polycrystalline sample of the same dimensions⁷⁰. At a primary beam energy of 6 keV, they measured gains of 2-3, the same order of magnitude as Yater et al.'s later experiments. At a higher primary beam energy of 8 keV, they measured a gain of 30, which is considerably higher than other measured transmission yields. However, in their experimental setup they consider all electrons emerging on the other side of the diamond film to be secondary electrons, rather than making clear the distinction between primary electrons which have passed straight through the film and 'true' secondary electrons.

Yater et al. measured secondary electron yields for reflection and transmission modes of two boron-doped, polycrystalline diamond samples on silicon substrates: one 2 μm thick with 'medium' doping, another 5 μm thick with 'heavy' doping⁷¹. They found no secondary electron transmission below primary beam energies of 5 keV, but attributed this to the 0.25 μm nucleation layer on the surface of the diamond film. The high concentration of grain boundaries and defects within the layer scatter and trap secondary electrons, and was thus attributed to non-existent yields at comparatively low primary electron beams (the highest energy beam used was 20 keV) due to the defects within the nucleation layer. Secondary transmission yields measured were between 1 and 3, but for reflection were much higher, with a δ of 12.

Yater et al. later tested a boron-doped, 150 nm film. The much thinner film gave much higher values for secondary electron yields, and at lower energy primary beams: δ values were 0.2, 1 and 5 at primary beam energies of 3 keV, 4 keV and 5 keV respectively⁷². Their experiments on the thin film stopped at 5 keV as the primary beam energy, as at higher energies the high energy electrons started transmitting straight through the diamond film, thus no longer giving a 'true' secondary electron yield. Typically in the literature it is noted that the primary beam energy for transmission mode measurements needs to be considerably higher (up to 20 keV) than the beam energies used in reflection mode, but it is often for samples of the same thickness (microns) as those used in reflection.

A comparison of reflection and transmission mode secondary electron yields was made by Dvorkin et al., using a theoretical model to predict the yields. The accuracy of the model was further validated by experimental measurements⁷³. Their model gave predictions for the primary beam energy needed for the maximum secondary electron yield, and for the maximum secondary electron yield in a transmission mode configuration. The two equations used are shown in Equations 7 and 8, and gave a δ of 3-7 for primary beam energies of 15-30 keV. A separate equation was given for maximum secondary electrons in reflection configurations, which is omitted from this review. However, solving the equations for the particular sample tested gave a yield of 19 for a primary electron beam of 1 keV in reflection experiments.

$$E_m = 17.2d^{0.625} \quad \text{Equation 7}$$

$$\delta = \frac{BE_0}{3E_{gap}} \left[e^{-\left(\frac{d-L}{z}\right)^{1.9}} - e^{-\left(\frac{d}{z}\right)^{1.9}} \right] \quad \text{Equation 8}$$

In Equation 7, E_m is defined as in Figure 6, and d is the membrane thickness. In Equation 8, B is the probability of an electron escaping the surface, E_{gap} is the bandgap energy, L is the carrier diffusion length and z is the distance from the surface. The results from the experimental setup used by Dvorkin et al. gave a maximum yield of 18 for a primary incident beam with a 950 eV energy in reflection mode, and a transmission secondary electron yield of 4 for a primary beam with energy 25 keV with films of 5 μm thick. The reflection results are within 10% error, and the transmission results lie within the range predicted by the model.

Dimitrov et al. implemented an integrated model for secondary electron emission, using the commercially-available VORPAL computational framework for secondary electron generation, transportation and emission^b. They estimated the transmission electron gain (the number of secondary electrons reaching the surface of the diamond, connected to a metal contact) by counting the number of free electrons which leave the diamond surface⁷⁴. Qualitative agreement was found between previous experimental results and the simulations for secondary electron yield; an increase in the maximum gain was found as the primary beam energy increased. However, experimental results were for the total transmitted gain, rather than the secondary electron gain. These transmission gain results were found to be accurately described by Equation 9⁷⁵.

$$G_t[E_p, E_f(t)] = (aE_0 - b)(1 - e^{-cE_f(t)}) \quad \text{Equation 9}$$

^b <https://www.txcorp.com/vsim-all-about-vsim>; accessed 10/02/2014

In Equation 9, G_t is the transmission gain, $E_f(t)$ is the time-dependent internal field, and a, b, c are coefficients with values chosen to best fit the previous experimental results. Further simulation work found that three-dimensional simulation of the results was only accurate if conservation of momentum of the electrons in the emission plane and the effective mass anisotropy of the lowest conduction band are accounted for⁷⁶.

1.6 Aims of the Project

The aim of the project was to investigate the secondary electron yield of diamond films in both reflection and transmission mode using a custom-built setup in the University of Bristol Diamond Laboratory. Once configured, the setup was to be used to measure the secondary electron emission of six diamond films of various thicknesses to determine the effect of film thickness on secondary electron yield.

A secondary part of the project was to use free-to-download Monte Carlo software to simulate the transport of electrons through the diamond film. The software could also be used to predict when the primary electron beam had completely permeated through the sample in transmission mode experiments, and as a way to determine the work function of the diamond films.

2 Experimental

2.1 Samples

For the experimental work, six samples of different thickness of diamond grown on silicon were provided by Applied Diamond, Inc., a USA based company which specialises in providing single crystal and CVD-grown polycrystalline diamond wafers for a variety of uses^c. The samples provided were CVD-grown, undoped diamond on 1 cm x 1 cm silicon wafers. Unfortunately, the exact nature of both the diamond and the silicon were unknown: the silicon may have been conducting or insulating, and the surface morphology of the diamond samples was thought to be either microcrystalline or nanocrystalline. It was assumed that all samples were the same and had been grown under identical conditions, the only difference in growth conditions between samples being the growth time to give the different thicknesses. The six samples had thicknesses of 20 nm, 35 nm, 60 nm, 80 nm, 120 nm and 150 nm. The thinnest sample tested in the literature for secondary electron yield in transmission was the 150 nm, boron-doped sample tested by Yater et al. in 2004⁷². As the samples were intended to be tested in reflection and transmission modes, the back of the silicon substrate was etched away to reveal the diamond grown onto the silicon, providing an

^c <http://usapplieddiamond.com/>; accessed 19/04/2014

approximately 2 mm in diameter hole through which transmission secondary electron measurements could be made. The six samples, as arranged on the sample holder for experiments, can be seen in Figure 11.

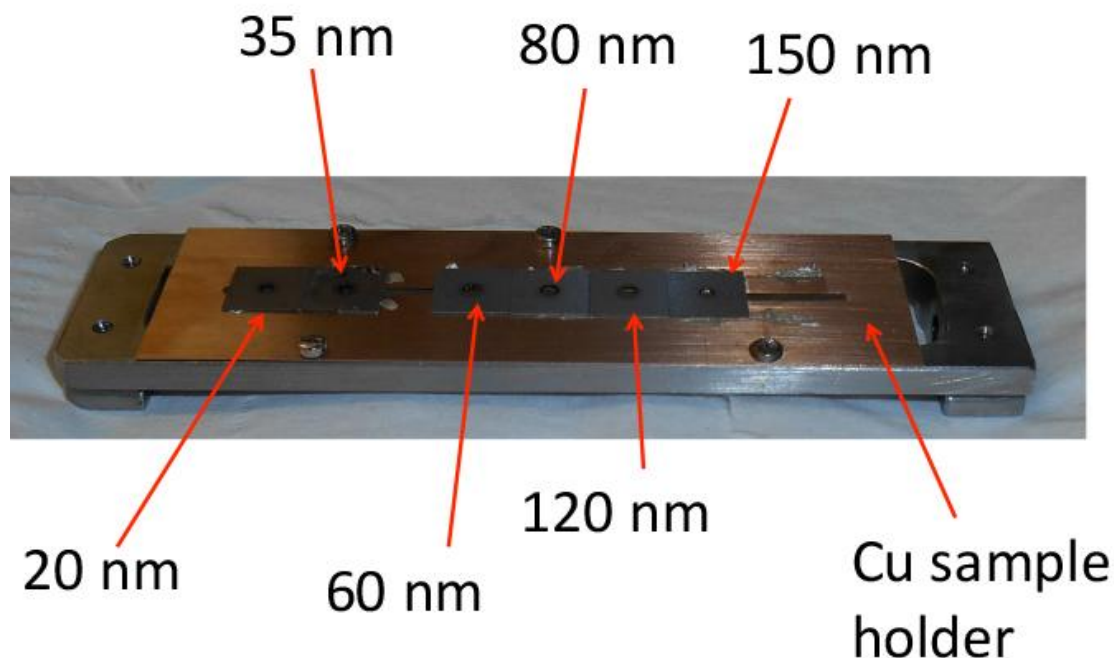


Figure 11: Photo of the sample stage and attached sample holder with the six samples to be used in the experiments. The copper sample holder has a line cut out down the middle which the diamond films can be lined up with to allow transmission measurements. The six samples, of varying thickness, were secured using conductive silver dag.

The six samples were arranged on the copper sample holder so the hole in the sample was aligned with the cut out in the sample holder. A conductive silver dag was used to secure the samples onto the sample holder before the sample stage was transferred to the secondary electron setup. As well as securing the samples, the dag would ensure good contact between the sample and the sample holder, which would help to dissipate any charge accumulated on the surface. The samples were stuck silicon side up; it was thought that by only exposing a smaller section of the diamond it might make it easier to locate the diamond window for experiments once the samples were sealed inside the vacuum chamber.

2.2 Experimental Method

The secondary electron experiments were carried out using a custom-built piece of apparatus developed by Raquel Vaz during her PhD work at the University of Bristol¹⁷. The setup designed was a large vacuum chamber kept under 10^{-7} Torr vacuum using a turbo pump, in which a sample stage

sat vertically beneath a Kimball Physics EGL-2022 electron gun. Any secondary electrons emitted struck phosphor screens in reflection and transmission configurations, with photomultiplier tubes to collect the intensity signals. Photos of the complete setup can be seen in Figure 12 and Figure 13.

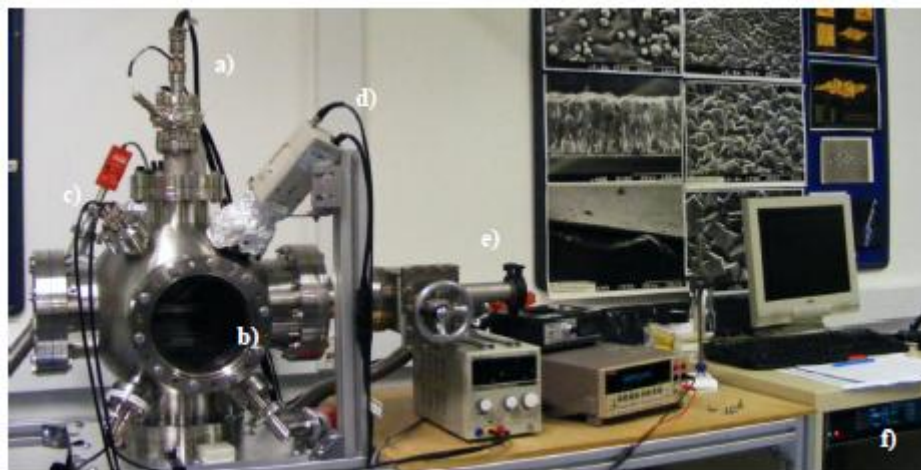


Figure 12: Front view of the secondary electron setup developed by Vaz in the University of Bristol Diamond Laboratory. The labelled components in the photo are as follows: a) electron gun, b) visual port for alignment of samples before measurements, c) connections for screen and stage biasing (if needed), d) camera (not used in these experiments), e) loading port, and f) electron gun control box.

Photo credit Vaz (2013)¹⁷.

In Figure 12, the electron gun (a) can be controlled by the electron gun control box (f), but LabView software was developed for fully automated measurements. The electron gun had been fully calibrated prior to these experiments, and hence the LabView software could change all the settings on the electron gun concurrently. LabView software could also be used to monitor outputs in the case of manually controlling the electron gun. The visual port (b) was covered during experiments with phosphor screens to avoid light from outside the chamber reacting with the phosphor. The loading port (e) allowed samples to be removed without bringing the entire system up to air.



Figure 13: Side view of the secondary electron vacuum chamber, showing the various ports connected to the chamber and their uses. The labelled components are a) the electron gun, b) holder for photomultiplier tube for reflection measurements and c) covering around port to ensure light did not enter the vacuum chamber, d) holder for photomultiplier tube for transmission measurements, e) visual port (here covered with foil), and f) the connection to the turbo pump keeping the system at vacuum. Photo credit Vaz (2013)¹⁷.

In Figure 13, holders for photomultiplier tubes can be seen for both reflection (b) and transmission (d) modes. During experiments, the phosphor screens emit light when electrons (backscattered, transmitted primaries and true secondaries) strike the screens. An intensity signal is read by the photomultiplier tubes, which is then recorded by LabView software on the computer.

Within the setup were several screens for measuring secondary electron emission. Initially both the single reflection screen and two transmission screens were phosphor screens, which would emit light when an electron struck the surface. The inside of the main chamber can be seen in Figure 14.

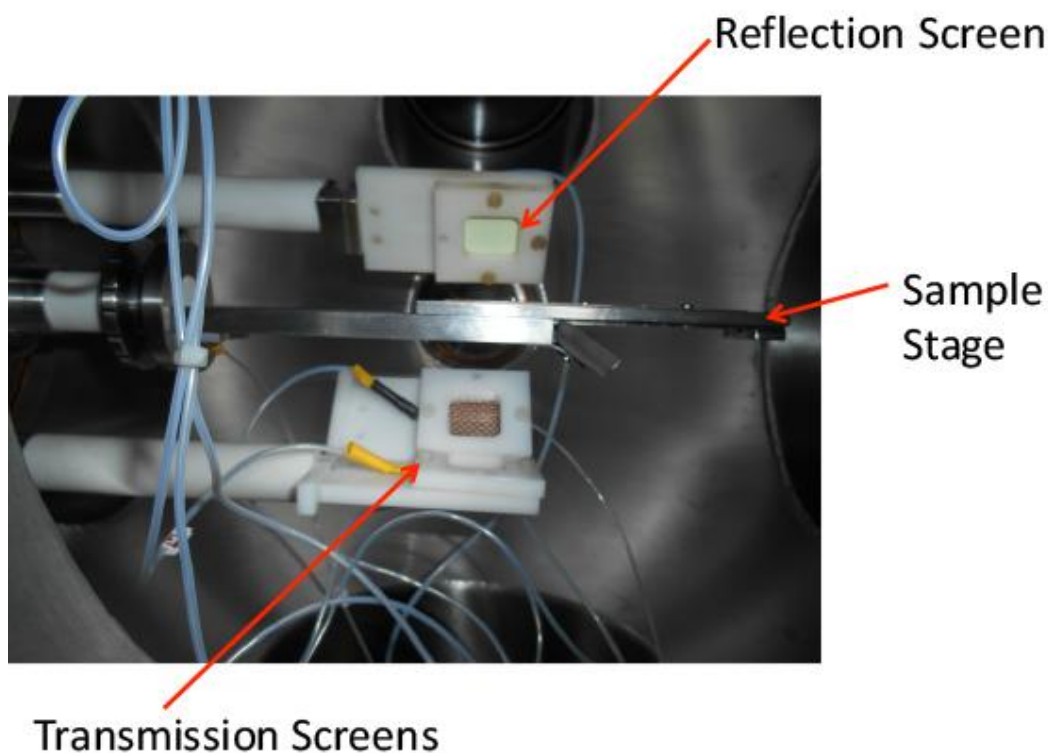


Figure 14: Inside of the chamber custom-built secondary electron emission setup. The system is typically under 10^{-7} Torr vacuum. An electron gun is positioned vertically above the sample stage, and the secondary electrons are collected at the reflection and transmission screens. Here the reflection screen is a green phosphor screen, while the transmission screens are copper plates.

In Figure 14, the stage holder (on which the sample stage is placed), the reflection screen and the transmission screens are all supported on the same plate, secured on the side of the chamber. This can be removed from the setup to allow easier alterations to the screen configurations. The sample stage can be removed from the stage holder while the system is under vacuum and then completely removed from the system using the loading port, allowing the samples to be changed if necessary without bringing the whole system up to vacuum.

The reflection phosphor screen was placed at 45° angle to the sample to try to collect only secondary electrons instead of other backscattered electrons from both inelastic and elastic collisions. Archard calculated the size of a “back-scattered cone”, a geometrical region of space into which backscattered electrons would be emitted³⁵. The higher energy electrons are expected to be emitted at small angles to the primary electron beam, and hence the 45° angle for the screen was chosen to collect the lower energy electrons, the majority of which should be true secondaries.

The second transmission screen was placed at a 45° angle to the first transmission screen, which was arranged parallel to the sample above it. The second screen was also covered by a copper mesh, which could be biased. By biasing the second screen at a low voltage (expected to be around 50 V), it was expected that the high energy transmitted primary electrons would travel straight to the first transmission screen and be collected there. Any low energy secondary electrons would be affected more by the biasing on the second screen and would therefore travel to the second screen instead, allowing separate measurements of transmitted primaries and emitted secondaries to be made. Biasing could also be used on the reflection screen, however previous work had shown that biasing the reflection screen was not necessary. A diagram showing the arrangement of the screens can be seen in Figure 15, where the screens, grids and sample are all grounded.

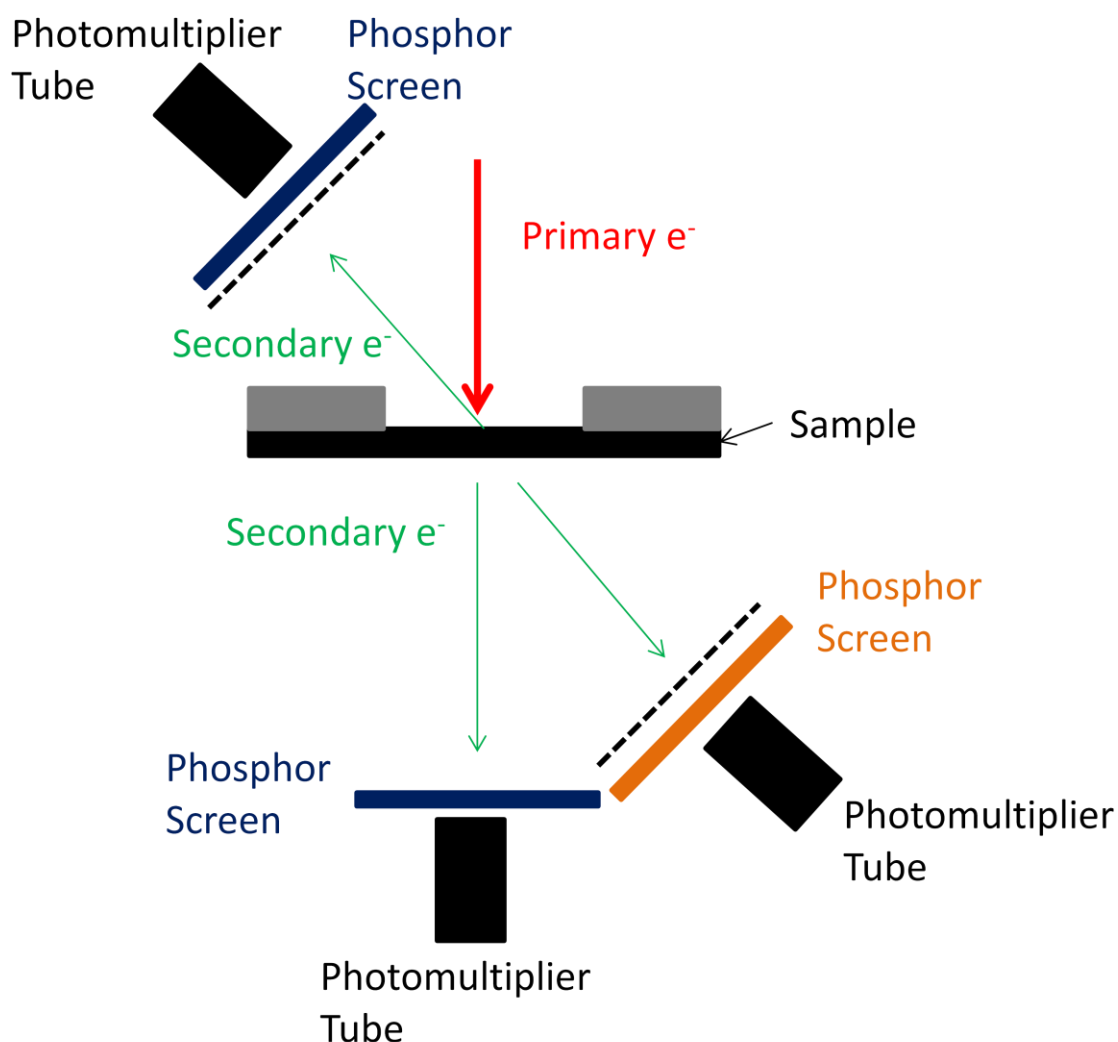


Figure 15: Arrangement of screens within the secondary electron setup, where dashed the black dashed lines near the angled reflection and transmission screens represent the copper meshes for biasing. Two different colour phosphor screens are used in transmission measurements.

In Figure 15, the two transmission screens are different colours to represent the different phosphors used. The two screens were made up using phosphors which emitted light in different regions of the visible spectrum: the primary electron screen (and also the reflection screen) would emit green light when the screen was struck by electrons, while the secondary electron screen would emit red light. The phosphor P15 (a self-activated zinc oxide phosphor, ZnO.Zn) was used for the emission of green light, while the phosphor P22R (a europium-activated yttrium oxide-sulphide phosphor, $Y_2O_3 + Fe_2O_3$) was used for the emission of red light. The phosphor screens were prepared by making up a suspension of the phosphor powder with deionised water, which was then deposited onto a glass screen using a pipette and left to dry. The glass screens had been pretreated with a thin layer of metal to prevent the phosphor screens charging.

2.2.1 Reflection Measurements

The reflection experiments were twofold. First, the entire sample area needed to be scanned in order to locate the diamond window. A fully automated LabView program known as Beam Scan was used, during which the primary beam voltage was set and the deflection voltage of the beam was altered in the x and y directions by the software. The intensity measurements from the photomultiplier tubes were recorded by the LabView program and the output file could be analysed using a separate LabView code to render the intensities as an image of the samples beneath the electron gun. The image was labelled with the x and y deflection voltages and hence the position of the samples could be read from the file.

Once the position of the diamond window was known, the deflection voltages could be set and a different LabView program, known as Energy Scan, could be used. This LabView program would aim the electron gun at the same area of the sample while sequentially increasing the primary beam energy of the electron gun from 200 eV to 5000 eV at intervals set by the user. The intensity of the light emitted by the phosphor screen was recorded by the software at every primary beam energy.

Before the results for the reflection measurements could be analysed, it was important to run a control sample through the Energy Scan program. For this purpose, a cleaned piece of copper was used. Assuming that the background signal, $S_{background}$, is much less than the intensity signal from diamond, S_{sample} , then the secondary electron yield can be calculated as a ratio of S_{sample} to the intensity signal from the copper, S_{copper} , as given in Equation 10¹⁷.

$$\delta = \frac{S_{sample}}{S_{copper}} \quad \text{Equation 10}$$

However, as detailed by Vaz when first calibrating the setup¹⁷, Equation 10 is valid as a relation for calculating secondary electron yield as long as a correction factor, $\delta_{copper}(E_x)$ is included. The correction factor is equal to the secondary electron yield for the copper reference sample at each primary beam energy, which can be found in the literature⁷⁷. So the secondary electron yield at a primary beam energy of E_x is given by Equation 11.

$$\delta = \frac{S_{sample}}{S_{copper}} \cdot \delta_{copper}(E_x) \quad \text{Equation 11}$$

2.2.2 Transmission Measurements

Once the position of the samples had been determined in reflection mode there was no need to rescan the samples in transmission mode using the Beam Scan program. Therefore, only the Energy Scan program was used during transmission experiments. Calibration proved to be more difficult for the transmission samples, as the collection of a reference signal as per reflection measurements was not a suitable method. Thick samples such as the copper used in the reflection calibration would emit few, if any, secondary electrons in transmission mode; regardless very little literature exists on secondary electron yields in transmission mode for thin samples which could be used as a reference. Therefore while transmission measurements were originally using the phosphor screens, the results could only be given as relative intensities and no results could be calculated for secondary electron yield using the phosphor screens in transmission mode. Alterations were consequently made to the setup so that copper screens could be used in place of the phosphors, and then Equation 1 could be used to calculate the secondary electron yield. Further issues with the transmission mode experiments are covered in Section 3.2.

2.3 Modelling Secondary Electron Emission

Further to the experimental work carried out, a search was carried out into the available software which can be used to model secondary electron emission. Monte Carlo codes are often used, having the advantage that in order to run for a certain sample no experimental data is needed (for example, escape depth of the electrons); the user-defined inputs such as sample composition are supplemented by empirical models which are more often than not built into free-to-use Monte Carlo based software⁷⁸. However, Monte Carlo simulations can take an excessively long time to run and statistical uncertainties cannot be eliminated if run for a finite time period⁷⁹.

2.3.1 Secondary Electron Emission Modelling Software

Both commercial and free-to-download secondary electron emission software is available, based on Monte Carlo methods. A selection of these are detailed below. It should be noted however that

when secondary electron yields are calculated, no distinction is made between secondary electrons transmitted through a sample and secondary electrons reflected from the surface.

2.3.1.1 Commercially Available Programs: CST Particle StudioTM and Electron Flight Simulator

Within the Computation Simulation Technology Particle StudioTM (CST PS) package, there is a mode within which secondary electron emission can be modelled^d. The CST PS is able to analysis particle dynamics in three dimensions, incorporating Furman's model for secondary electron emission and Vaughan's model for the secondary electron yield^e.

CST PS has been used by Hamme et al. to study secondary electron emission within the electron collector of a high power tube, and within a superconducting TESLA cavity⁸⁰. They found that the probabilistic-based model needs accurate fitting parameters to describe the material in order to get accurate simulation results, but that overall the simulation is a successful tool for analysing secondary electron emission. No papers were available which stated the use of CST PS for simulation of secondary electron emission from diamond films.

Electron Flight Simulator claims to be the most widely used Monte Carlo simulator of its kind^f, but while it can accurately model electron trajectories through a solid as a function of energy, hence giving a penetration depth value, it is geared more towards the simulation of x-ray generation rather than secondary electron emission. Figure 16 shows an example of the Electron Flight Simulator modelling capabilities for a BaTiO₃ sample.

^d <https://www.cst.com/Products/CSTPS/StationaryParticleTrackingSolver>; accessed 10/02/2014

^e <https://www.cst.com/Content/Media/CST-Charged-Particle-Simulation.pdf>; accessed 10/02/2014

^f <http://www.small-world.net/efs.htm>; accessed 10/02/2014

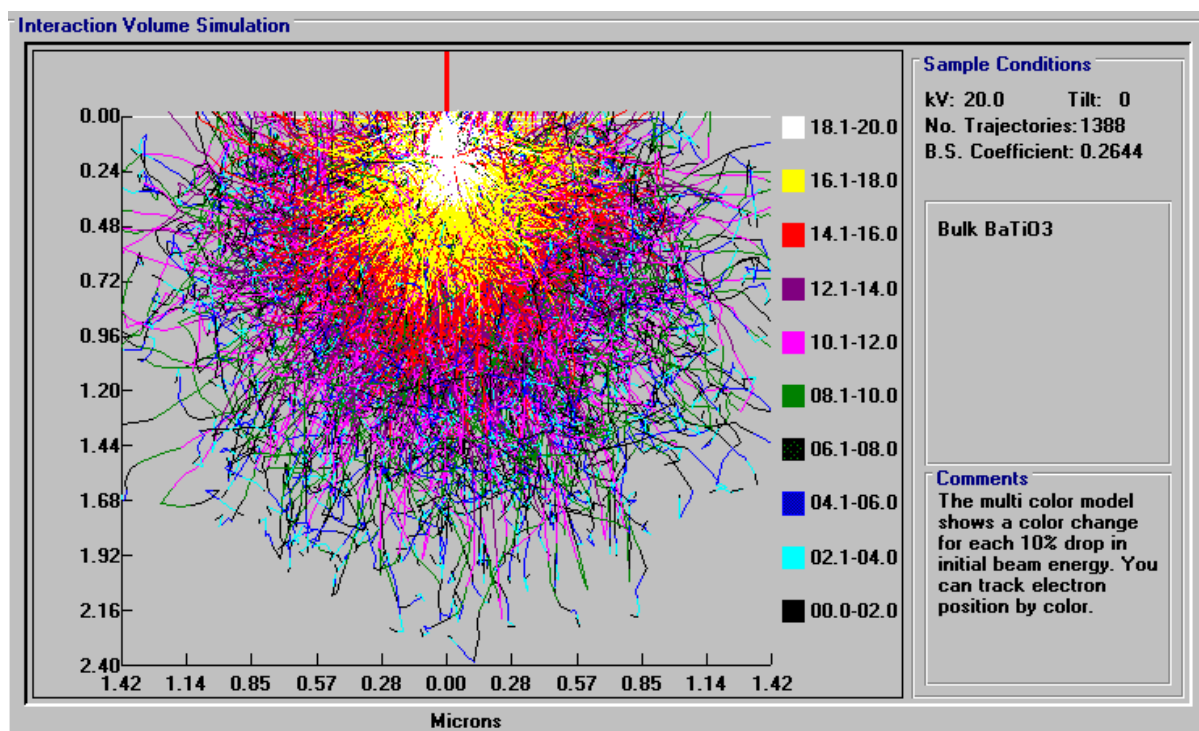


Figure 16: Example screenshot of electron trajectories mapped in BaTiO_3 , as shown on the Electron Flight Simulator webpage^g. The software is able to track the change in electron energy as they travel through the sample; the software is able to map a large number of trajectories but the software is geared more towards x-ray simulation.

2.3.1.2 NISTMonte and NIST DTSA II

The National Institute of Standards and Technology (NIST) has developed a Monte Carlo simulation known as NISTMonte, which has the capability to define complex sample geometries. NISTMonte models the generation and subsequent absorption or detection of x-rays, and also backscattered electrons, however the electron trajectory is no longer tracked once the energy of the electron reaches below 50 eV ⁸¹, and thus the software is not properly set up for secondary electron emission. A combination of NISTMonte and another software model called MONSEL allows NISTMonte to be used for secondary electron emission modelling, which gave a good match between experimental data found in the literature and the simulations for secondary electron yield⁸². However, this edited code is not available for free download. NISTMonte has been updated since 2005, when Ritchie⁸¹ originally described the program, to a new program known as NIST DATA II^h, but there is still no setup for secondary electron simulation.

^g <http://www.small-world.net/image7.gif>; accessed 10/02/2014

^h <http://www.cstl.nist.gov/div837/837.02/epq/dtsa2/index.html>; accessed 10/02/2014

2.3.2 CASINO

CASINO (abbreviated from monte CARlo Simulation of electroN trajectory in sOLids) is a widely used Monte Carlo simulation program used for the simulation of electron transport and scattering in bulk solids. Examples of using CASINO for secondary electron emission include studies by Praver et al. into the region around an ion impact where the secondary electron emission is suppressed, using electron-hole density information from CASINO simulations at different primary beam energies⁸³. Yater et al. used CASINO to investigate stopping distances of electrons with boron-doped nanocrystalline diamond films: they found a good match for the energy distribution in the sample and predicted penetration depth of the primary electron beam between the CASINO simulations and the energy-dependent electron range calculation⁶¹ (which was developed by Kanaya & Okayama).

Morozov et al. compared the results of Monte Carlo simulations from CASINO and another Monte Carlo simulator, Geant4, to their experimental results for electron energy distribution functions for 10 keV electron transmissions through 300 nm ceramic films⁸⁴. Geant4 is a simulation written in C++⁸⁵, with the capabilities to be adapted for simulations in x-ray astronomy and radiotherapy techniques, as well as secondary electron emission studies⁸⁶. Geant4 was found to provide energy distributions much closer to the values measured experimentally, with uncertainties of 3% for Geant4 compared to 8% for CASINO. They previously attributed to the discrepancies between experimental and theoretical results from CASINO due to the simulation not tracing the high energy secondary electrons⁸⁷. However Geant4 is a less intuitive software package involving a complicated setup and more knowledge of computing beyond the comparatively user-friendly CASINO.

To date, there are two versions of CASINO available for free download and use, a two dimensional version and a three dimensional version. Examples of simulations from both types are detailed in the next sections.

2.3.2.1 CASINO 2D

CASINO v2.4 was originally developed for scanning electron microscope techniques, particularly low-energy beam applications in bulk materials⁸⁸. It can also be used for backscattered electrons, and models the intensity of an electron beam as it travels through the sample, which gives an indication of whether or not electrons (either primary or secondary) would be transmitted through a thin film. Figure 17 shows the result of a simulation on a 60 nm diamond sample, where the primary beam has an energy of 2.5 keV.

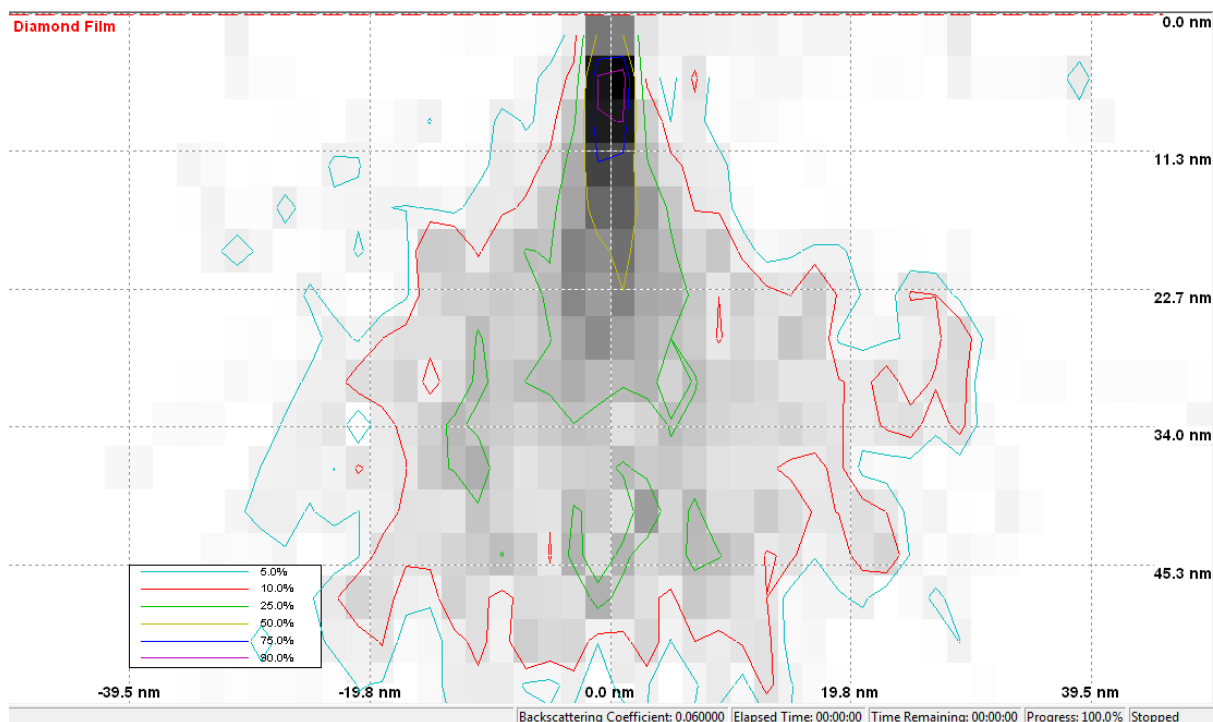


Figure 17: Screenshot of the energy distribution simulation of electrons from a primary beam of 2.5 keV on a 60 nm diamond film. The backscattering coefficient is given as 0.06 by the software, where the backscattering coefficient deals only with emerging from the sample with energies greater than 50 eV⁸⁹. The coloured lines represent the amount of energy the electrons in that region have left as a function of their primary energy: for example, the darkest shaded regions are surrounded by purple lines, suggesting that at this point in the sample, they still have 90% of their original energy.

Figure 17 shows the energy distribution of electrons within a 60 nm diamond film. Other graphical results also produced concurrently by CASINO v2.4 include backscattered and transmitted energies and the angle of backscattering. This version of CASINO does not have any built-in capabilities for secondary electron analysis, however it can be used to see whether or not any electrons would be expected to be transmitted through a sample. Figure 17 has regions of low energy electrons at the bottom of the sample, suggesting that some transmitted electrons would be expected for a primary beam of 2.5 keV.

2.3.2.2 CASINO 3D

CASINO v3 was developed in order to handle the simulation of electrons in complex, three-dimensional samples. Features such as user-defined, complex samples and secondary electron emission based on the Möller equation and Plasmon theory (for fast secondary electrons and slow secondary electrons respectively) were added to the software⁵⁶.

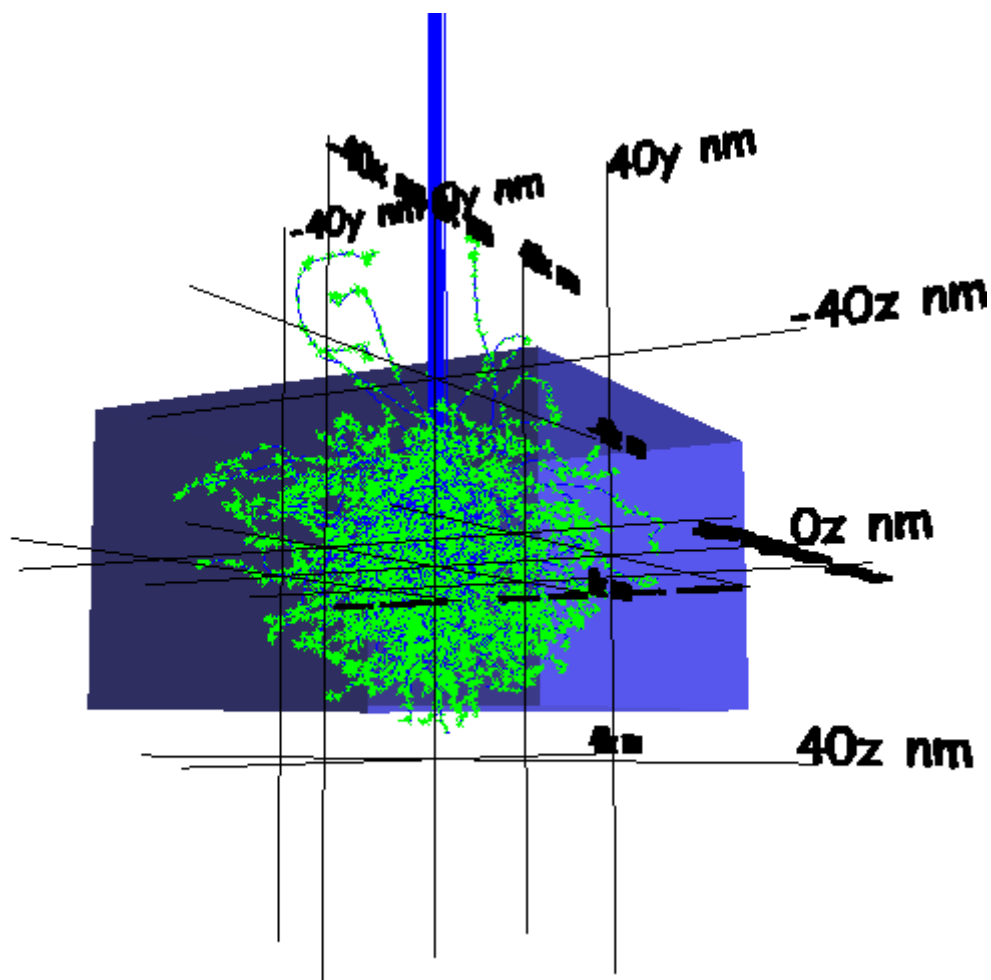


Figure 18: Screenshot of the 3D CASINO simulation for a 2.5 keV beam incident on a 60 nm diamond sample. The generated 3D image can be manipulated to different zoom levels and rotated to different views. A small number of electron trajectories can be seen on both the top and bottom surfaces of the sample.

Figure 18 shows the three-dimensional simulation of the sample simulated in Figure 17. Agreement can be seen between the two samples in that the two-dimensional simulation predicts some low energy electrons leaving the bottom of the sample, and in the three-dimensional simulation, a small number of electron trajectories can be seen leaving the bottom of the sample. However, while there are clearly some backscattered electrons, if not secondary electrons, escaping the surface, the software gives both the backscattered and secondary electron coefficients as zero.

While the software is able to handle three dimensional modelling and secondary electron generation, personal user experience of the software has been poor. Simulations take a large amount of computer memory, and only rarely finish calculations for secondary electron coefficients.

Furthermore, there is no specification for whether or not the secondary electrons generated are reflected from the surface of the sample or transmitted.

A combination of both CASINO 2D and 3D was used in the simulation study carried out as part of the project, due to the relative ease of software use compared to other free-to-download Monte Carlo software and the range of data the software could simulate. However, Monte Carlo simulation programs such as CASINO each sample as a homogeneous sample⁹⁰, free of defects, which affects the diffusion of the electrons within the sample and hence the secondary electron yields calculated.

3 Results and Discussion

As mentioned in Sections 2.2.1 and 2.2.2, the experimental work was undertaken in two parts. Originally the phosphor screens were in place, and measurements could only be taken from one phosphor screen at the time due to LabView programming. Therefore Beam Scan experiments were run in reflection mode to determine the positions of the samples, followed by Energy Scan in reflection mode and transmission mode for the phosphor screens. Alterations were later made to the setup to determine transmission secondary electron yield using copper plates instead of the phosphor screens.

3.1 Reflection Experiments

Once the x and y values were determined from the Beam Scan experiments, the Energy Scan program was used on all six samples in reflection mode and the intensity measured from the phosphor screens. Using the calibration process described in Section 2.2.1, the intensity signal was scaled against a copper reference sample and literature data for the secondary electron yield of copper at a series of energies, where the maximum yield from copper is 1.43 at 500 eV⁷⁷. The scaled secondary electron yield plots can be seen in Figure 19, and the secondary electron yields are given in Table 4.

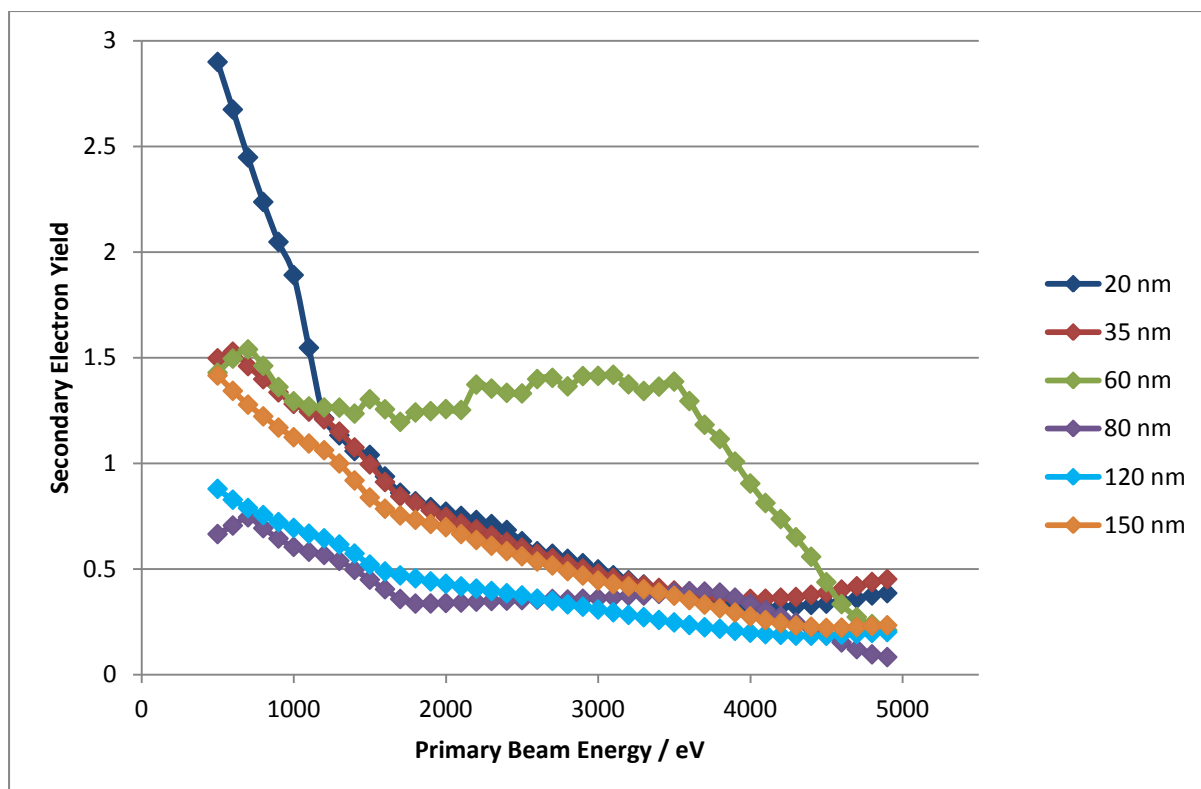


Figure 19: Secondary electron yield curves for all six samples as a function of primary beam energy. All samples peak at lower primary beam energies, however the calibration data is not available for energies below 500 eV and hence the peak may in fact be at lower energies. The 60 nm sample exhibits a broad peak at higher energies before the yield rapidly decreases from 3400 eV onwards.

Sample Thickness / nm	Secondary Electron Yield	Peak Position / eV
20	2.90	500
35	1.53	600
60	1.54	700
80	0.79	700
120	0.88	500
150	1.42	500

Table 4: Secondary electron yields and the primary beam energy each peak appears at for each sample. The three samples where the peak position appears at 500 eV may have peaks at lower energies (200 eV – 400 eV), however calibration data are not available for this range of energies.

Figure 19 and Table 4 show a general trend with the secondary electron yields and thicknesses: the thinner samples tend to give higher yields. The trend would certainly be expected in transmission mode, as in the thinner samples the excited secondary electrons have less distance to travel to the transmission emission surface and therefore less chance of being reabsorbed into the sample. A

dependence of secondary electron emission on sample thickness has been found³⁰, for thicker samples than those tested (comparing 100 nm to 4 μm) and for diamond grown on substrates rather than diamond windows. The argument given by Ternyak et al. is that the thicker films are less conductive and so thinner films allow the electrons to move through the sample better and are emitted easier; however this is a comparison of μm thick films to nm thick films and for boron-doped samples. Nevertheless, a dependence on film thickness can be seen.

While the values of secondary electron yield quoted in Table 4 are given as the reflection secondary electron yields, for diamond windows it is expected that some of the generated secondary electrons will have been emitted from the transmission surface rather than the reflection surface. However, as secondary electrons emitted from the transmission surface have to travel further through the sample, it is expected that the secondary electrons emitted from the transmission surface while measuring reflection yields are a fraction of the total number of secondary electrons generated in total. In order to confirm this, a useful comparison would be between the samples here and samples with the same characteristics grown on a silicon substrate. It is not possible to carry out this experiment in the current setup as the diamond grown on the silicon is on the underside of the sample once it is stuck to the sample stage.

The broad second peak for the 60 nm sample is completely unexpected. However, later experiments found out that the beam deflection towards the spot does not have same coordinates at different energies as the deflection to a point is done by voltage. The second peak could be due to silicon secondary electron peak (which is unlikely as the secondary electron peak for silicon is at low primary beam energies of around 450 eV⁵⁵) or backscattered electrons. The 45° angle screen was chosen on assumption that any inelastic/elastically scattered electrons would have enough energy to be reflected at small angles to the primary beam, providing the beam is vertical. So if the primary beam is deflected by a large amount, the angle it hits the sample at could cause more backscattered electrons to hit the phosphor screen, resulting in the second peak at higher primary beam voltages.

3.2 Transmission Experiments

Two sets of phosphor experiments were carried out: one involving phosphor screens and one involving copper plates. Originally the setup shown in Figure 15 was used, with the intensity measured from the screen directly beneath the sample. While running these experiments confirmed that the setup worked, all transmitted electrons were measured, which would be a mixture of low energy true secondary electrons and transmitted, high energy primary electrons. The data from these experiments are presented in Section 3.2.2, but it should be noted that there was no available

calibration for transmitted secondary electron yields and therefore the data presented are intensities only.

The setup was brought up to air and dismantled in order to place the second phosphor screen into the holder and test the electronic connections, ensuring everything was grounded. However, before the setup was reassembled, it was decided that the phosphor transmission screens would be replaced with copper plates. By using copper plates, the secondary electron yield could be calculated directly from the primary beam emission current, as controlled by the electron gun control box, and the current from the transmission screen as recorded by a multimeter.

3.2.1 Transmission Simulations

One of the advantages of CASINO 2D over its 3D counterpart is the ability of the software to display the electron energy distribution throughout a slice of the diamond sample. CASINO 2D was used to simulate the electron energy distributions for all six samples, with primary beam energies from 0.1 keV to 5 keV in steps of 0.1 keV. These simulations were run to give an estimate of when transmitted primary electrons could start striking the phosphor screens or copper plates as they were being emitted at the same time as the secondary electrons. The results from these simulations, plotted as a graph of primary beam energy for transmission against diamond film thickness, are shown in Figure 20.

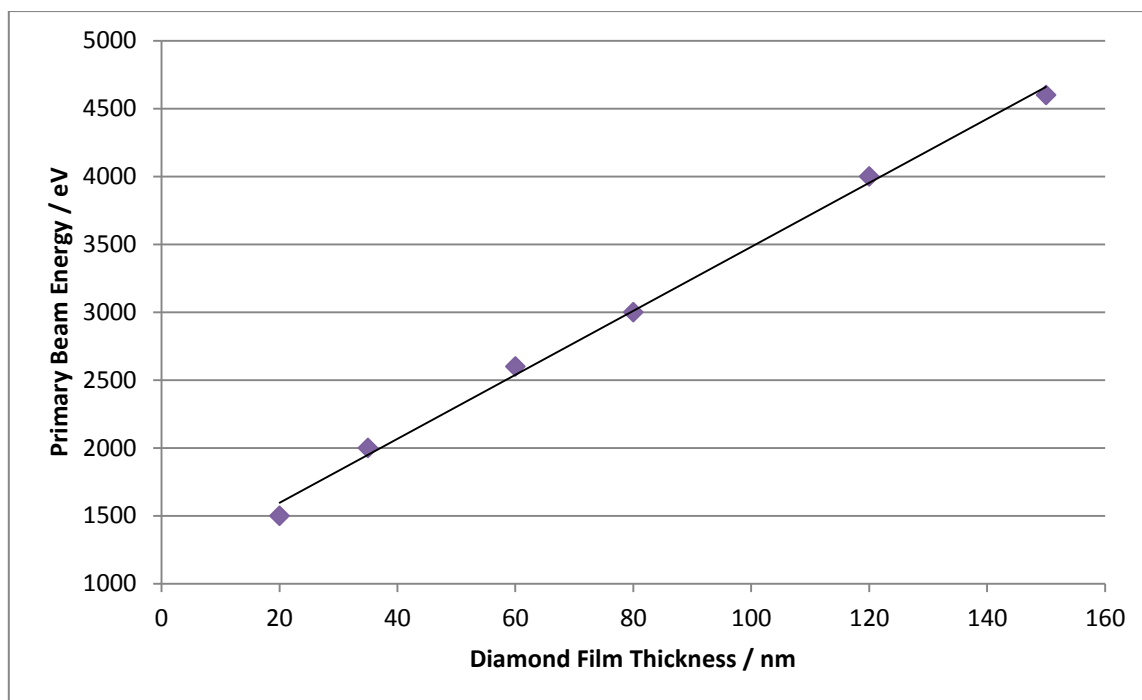


Figure 20: Graph of simulation-predicted primary beam energies needed for primary electron transmission against diamond film thickness. In CASINO 2D, the ability to change the work function of the sample is unavailable, so it is assumed to be the same as the value set in its 3D counterpart, where the work function is automatically set at 5.5 eV. The simulation results give a straight-line relationship between film thickness and primary beam energy. The R^2 value is 0.9969, setting the y intercept to zero gives a lower R^2 of 0.7126.

Figure 20 shows a straight-line relationship from the data as plotted, showing that thinner films will start transmitting primary electrons at much lower primary beam energies, which would be expected. Experiments from literature tend to carry out transmission experiments at much higher primary beam energies, typically between 10 keV and 20 keV, but the simulations show that the 5 keV limit on the electron gun is more than sufficient for the much thinner films. Even without biasing the second screen, it should still be possible to measure some secondary electron emission on the planar screen for several primary beam energies before transmitted primaries start to be measured as well.

In Figure 20, while most of the points fit the line, the 20 nm point lies slightly below the line of best fit. Further simulations were carried out on thinner samples than those tested to see what the relationship was between the primary energy needed for transmission and film thickness for samples of 10 nm thickness or less. The results are shown in Figure 21.

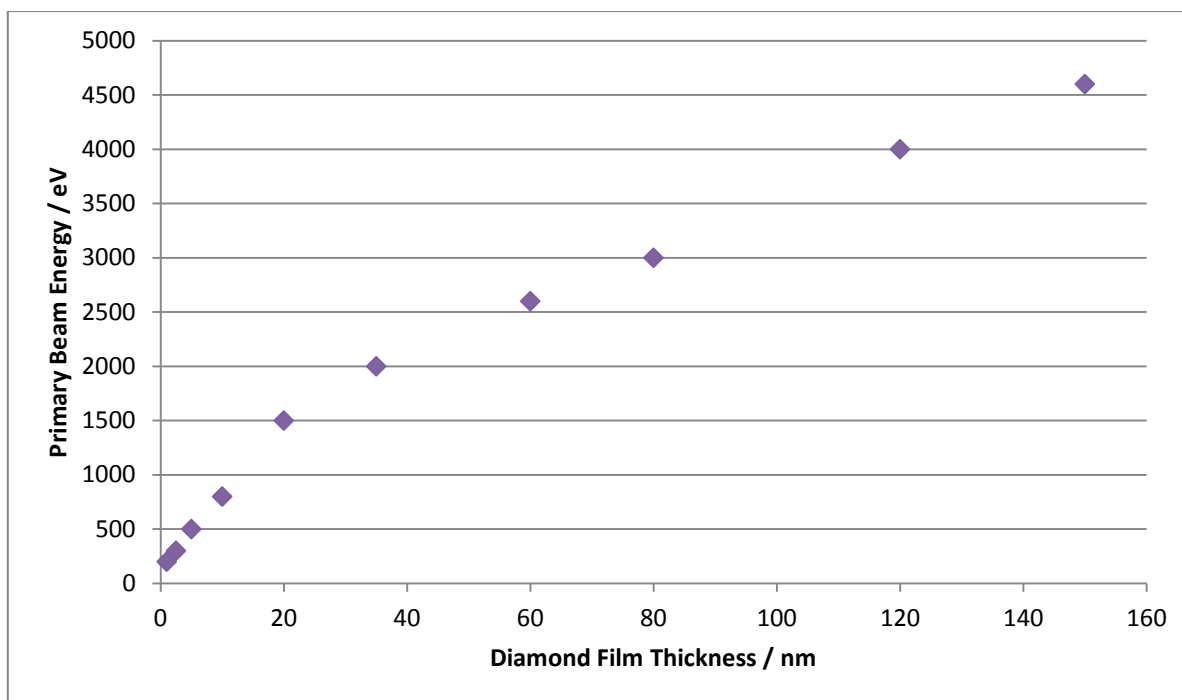


Figure 21: Graph of primary beam energy needed for primary electron transmission as a function of diamond film thickness, as predicted by the Monte Carlo simulation program CASINO 2D. A non-linear relationship can be seen between primary beam energy and film thickness for film thicknesses of 10 nm or less.

In Figure 21, the addition of simulation results from films of 10 nm, 5 nm, 2.5 nm and 1 nm thickness can also be seen. Unlike the results from thicker films, there is a non-linear relationship between film thickness and primary beam energy for these thinner films, predicting a decrease which may eventually lead to a point lying on the origin. To confirm any relationship between primary beam energy and diamond film thickness, further simulations should be carried out for thicker films to see if the linear relationship continues for films thicker than 35 nm.

3.2.2 Phosphor Screen Experiments

Once the Beam Scan program had been used to locate the hole, transmission Energy Scan experiments were run for the six diamond samples using the planar phosphor transmission screen to measure secondary electron emission. No biasing was applied to the copper mesh across the screen, and the beam current was kept constant for all experiments at 3.0 μA . The intensity results for the samples can be seen in Figure 22.

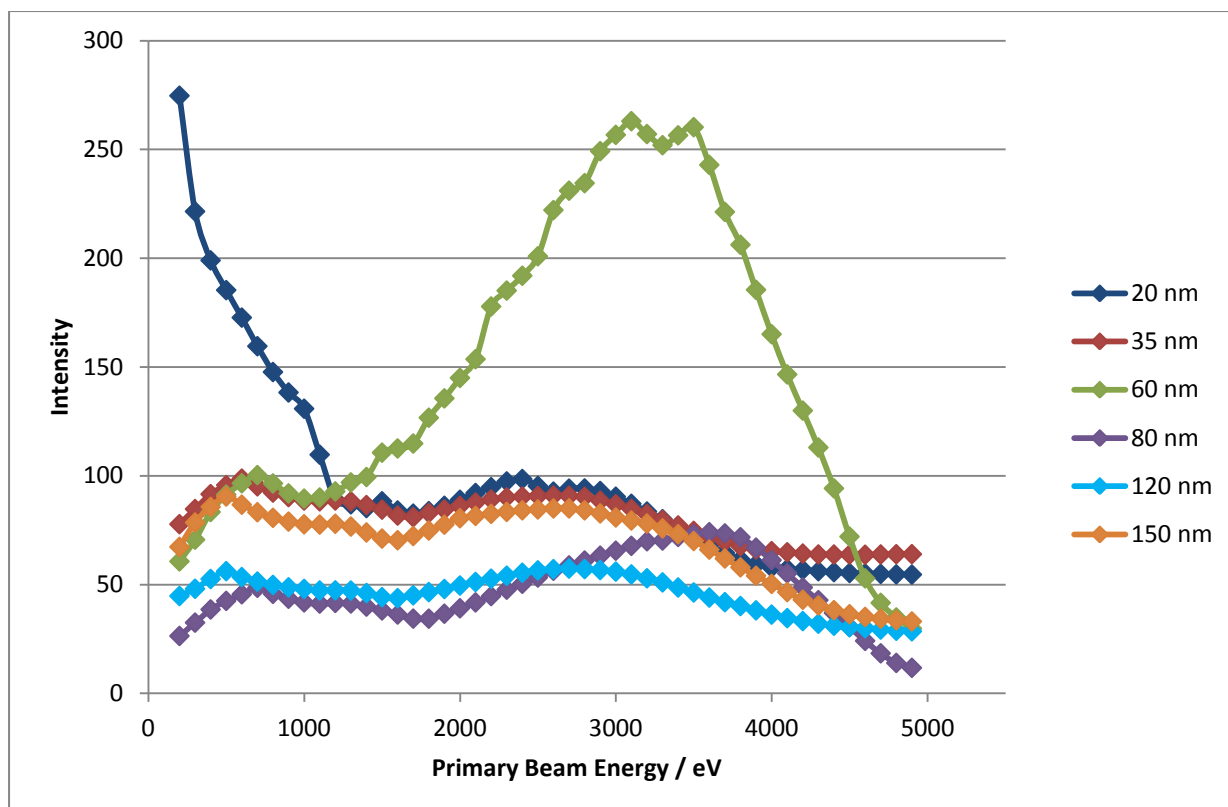


Figure 22: Plot of the measured intensity of secondary electrons in arbitrary units against the primary beam energy. The secondary electron intensity peak stays between 500 eV and 700 eV regardless of the thickness of the diamond film. A much higher peak can be seen for the 60 nm sample, with the highest intensity measured at 3500 eV.

Figure 22 shows the measured intensities of electrons striking the phosphor screen as a function of primary beam energy. The samples all have secondary electron peaks in the same area, with the highest peak of 274.7 for the 20 nm sample, which would be expected as the thinner the sample, the less distance secondary electrons have to diffuse through the sample to reach the transmission surface and hence there is a much smaller chance that these low energy electrons will be reabsorbed into the diamond lattice. However, this reasoning would suggest that the thickest sample, 150 nm, would have the smallest secondary electron intensity. Instead, the 80 nm sample has a much lower intensity peak of 51.4. The peak intensities for each sample are detailed in Table 5.

Sample Thickness / nm	Peak Intensity	Peak Position / eV
20	274.7	700
35	98.7	600
60	103.2	700
80	51.4	500
120	56.2	500
150	85.7	400

Table 5: Peak intensities and the primary beam energies the peaks were generated at for each of the six samples. The peak intensity tends to decrease with increases in the thickness of the samples, with the exception of the 150 nm sample, which has the fourth-highest measured intensity, and the 80 nm sample, which has the lowest intensity.

From both Table 5 and Figure 22, the intensity peaks are at low primary beam energies, and there is a general trend of decreasing intensity with increasing sample thickness. Both 80 nm and 120 nm have far lower intensities compared to the other four samples. While they are expected to have lower intensities than the thinnest samples, the intensities are considerably lower than the other intensities. As mentioned previously, when Energy Scan is used the set x and y deflection values move the primary electron beam different amounts as the primary beam energy increases. If the primary beam was not striking the centre of the window originally, then a smaller proportion of the electrons in the primary beam would be striking the diamond to excite secondary electrons. Therefore, an error in positioning of the beam could explain why the 80 nm and 120 nm sample results are so much lower than the other four samples.

All of the samples have a second peak starting at about 1500 eV, most noticeable in the 60 nm sample. While for the 20 nm sample, this could be the start of primary electrons being transmitted (as predicted by the simulation results from Figure 20), the appearance of the second peak is too low for the other samples for the cause of the peak to be primary electrons. The consequent decrease in measured intensity suggests that primary electrons may not be the cause, and there may be a fault in the setup. If high energy primaries were being transmitted and measured, the measured intensity would be expected to increase with consequent increases in primary beam energy.

The large peak for the 60 nm sample is unexpected, and while primary electrons may be transmitted at beam energies above 2600 eV and the peak is at 3400 eV, the sharp increase starts at 1700 eV, which is around the same energy at which other samples exhibit the second, smaller peak. A sharp increase could be due to damage to the film, causing it to break and allowing a 'clean' path for the primary electron beam to strike the phosphor, however if the film had broken during experiments

the intensity would not be expected to decrease again as the primary electron beam energy continued to increase. The sample diamond window was therefore thought to still be intact, so the anomalous peak could be explained by the electron beam moving so drastically away from the diamond window that it was in fact travelling directly through the line in the sample holder next to the sample, as there was a gap between the 35 nm and 60 nm samples (see Figure 11). The decrease in intensity could be due to the deflection of the beam reaching the edge of the next sample, or the edge of the slit in the sample stage, resulting in a smaller proportion of the electrons being transmitted. However, a similar peak appeared in the reflection data (see Figure 19), and it could be argued that there may in fact be a fault with the sample, or contaminants present, however it is interesting that there only seems to be an effect at higher energies, as both the reflection and transmission experiments exhibit a secondary electron peak in the same region as the other samples. The appearance of the secondary electron peak in the same region for each sample would be expected, as the doping and surface termination of each sample is the same, it is only the sample thickness that has changed.

Regardless of the second peaks, the preliminary phosphor screen experiments show that the setup is suitable for measuring secondary electron emission in transmission mode. As a suitable calibration was unavailable for transmission mode experiments with phosphor screens, the equipment was dismantled and a different experimental setup tested.

3.2.3 Copper Screen Experiments

After preliminary experiments were run using the phosphor transmission screens, the setup was updated to use copper plates instead. By using copper plates, no further calibration was needed as the secondary electron yield became a ratio of the set primary beam current and the measured secondary electron current from the transmission screens. The new experimental setup is shown in Figure 23.

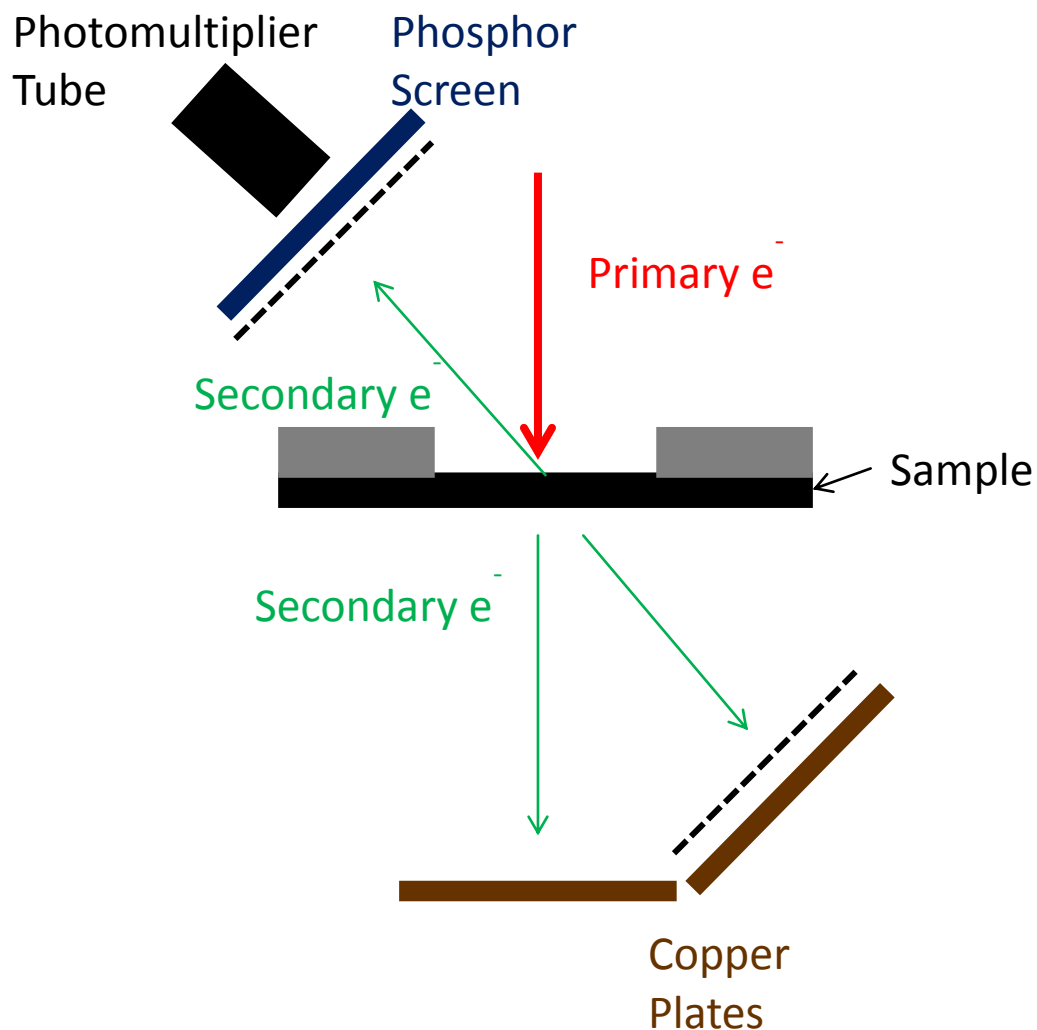


Figure 23: Diagram showing the arrangement of the screens after removal of the transmission phosphor screens and their consequent replacement with copper plates. The dashed lines represent the copper meshes. While not shown, the copper plates could be connected up to an external multimeter, from which the current generated from electrons striking the copper surface could be read.

Both copper plates in Figure 23 were grounded and connected by a series of wires inside the vacuum chamber to external ports on the chamber to allow connections of the plates to multimeters. Currently the LabView Energy Scan program is only configured to read phosphor screen intensities and thus the current produced by emitted electrons was measured manually from the multimeter. However, upon replacing the screens inside the setup and running Beam Scan in reflection mode to determine the position of the samples, several experimental issues began to arise, as detailed in Section 3.2.3.1.

3.2.3.1 Experimental Issues

After the copper screens were placed inside the setup and the chamber brought back down to vacuum, new Beam Scan experiments were run in reflection mode to determine the position of the 20 nm and 35 nm samples, which were currently placed under the electron gun. It was expected that fairly clear images would be produced, which would allow easy location of the hole on the sample substrate. The image produced for a Beam Scan at a primary beam energy of 1200 eV is shown in Figure 24, which is far less clear than expected.

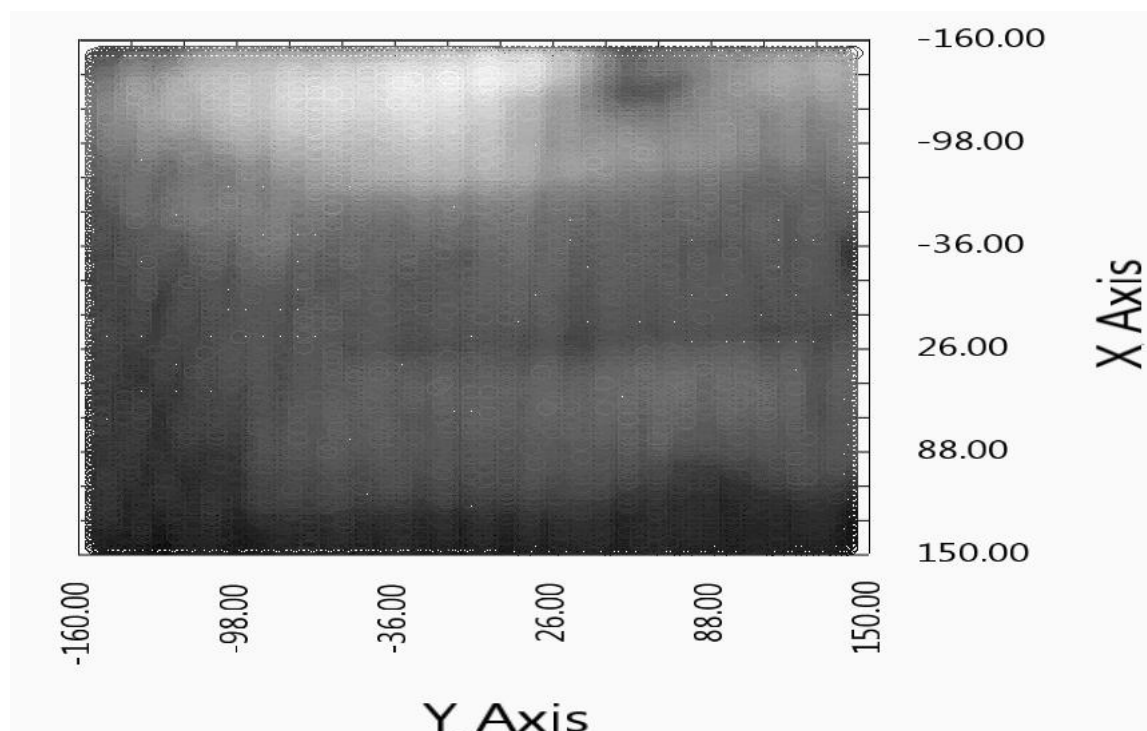


Figure 24: Screenshot of analysed data outputted from Beam Scan LabView program to determine the location of the 20 nm and 35 nm samples at 1200 eV primary beam energy. While two darker areas can be made out indicating the possible location of the samples, the hole is not well enough defined to allow a precise estimation of its location along the sample stage. The x and y coordinates here correspond to the deflection voltage applied to move the beam to a particular location.

Figure 24 is very blurred, and it is difficult to determine many features of the samples and substrate holder. The much lighter area in the top of the image is likely to be the edge of the metal substrate holder, which would deflect a lot of electrons. The bottom of the image, where it is much darker than the rest of the image, indicates the area beyond the sample holder. Likewise, the location of the hole in the silicon substrate would be expected to be clearly a lot darker than the surrounding silicon. However, it is difficult to discern the two samples, let alone the holes in the substrate with any certainty. The hole on the left sample is faintly visible, but not with any clarity to guarantee that

the centre of the hole would be directly beneath the primary electron beam, hitting the edge of the silicon etching would lead to error in the results.

A couple of reasons were suggested for the poor quality of the Beam Scan. First, it was thought that perhaps during the dismantling of the chamber that some dust had been attracted to the electron gun filament. Despite covering the opened ports of the main vacuum chamber while the new screens were being fitted, it is possible that some dust entered the system when the screens and sample holder was replaced inside the chamber. The primary beam voltage and the primary beam current were both increased, with the idea that the increased voltage and current would burn any impurities off the filament, and thus the clarity of the images would be improved.

The image clarity failed to improve after twelve runs, where the beam voltage was increased up to 1500 eV (however the higher voltage was found to decrease the quality of the image further) and the beam current increased up to 8.7 μA . Despite the prolonged increase in voltage and current, carried out over the course of a week, the image quality did not improve. Any dust should have been burnt off the filament, and so a new solution was needed. It was suggested that the filament may have burnt out and need replacing; however as an idea this was held as an absolute last resort. A large amount of time would be lost recalibrating the settings needed for optimum beam characteristics at each primary beam energy step, and therefore it was decided to try other methods for improving the Beam Scan image.

As the exact properties of the silicon substrate were not known, it was thought that the silicon could actually be charging and then discharging randomly, causing the blurs in the image. For secondary electron emission experiments, a substrate needs to have good conductivity properties to allow excess charge to move to the metal sample holder and away from the sample surface, thus preventing surface charging⁶⁹. One of the most common methods of reducing surface charge is often used in Scanning Electron Microscopy (SEM), involving the coating of the sample with nm-thick layers of metal, typically gold or silver⁹¹. It was decided that one of the mid-thickness samples, either 60 nm or 80 nm would be coated with a silver coat of several nanometres. The effect of the silvering on the film was unknown, the films are quite thin and delicate and it was unknown whether or not the silvering process, carried out in the Electron Microscopy Unit at the University of Bristol, would damage the film.

The sample stage was carefully removed from the vacuum chamber, but unfortunately the 60 nm, 80 nm and 120 nm were loose on the stage. The 60 nm sample was chosen for silver coat, and after silvering the 60 nm sample and the 120 nm sample were compared under an optical microscope.

The 80 nm sample film looked like it had been damaged and no film could be seen, however a blue reflection could be seen in the window on the 120 nm sample so this sample was chosen for comparison. Images from the microscope can be seen in Figure 25.

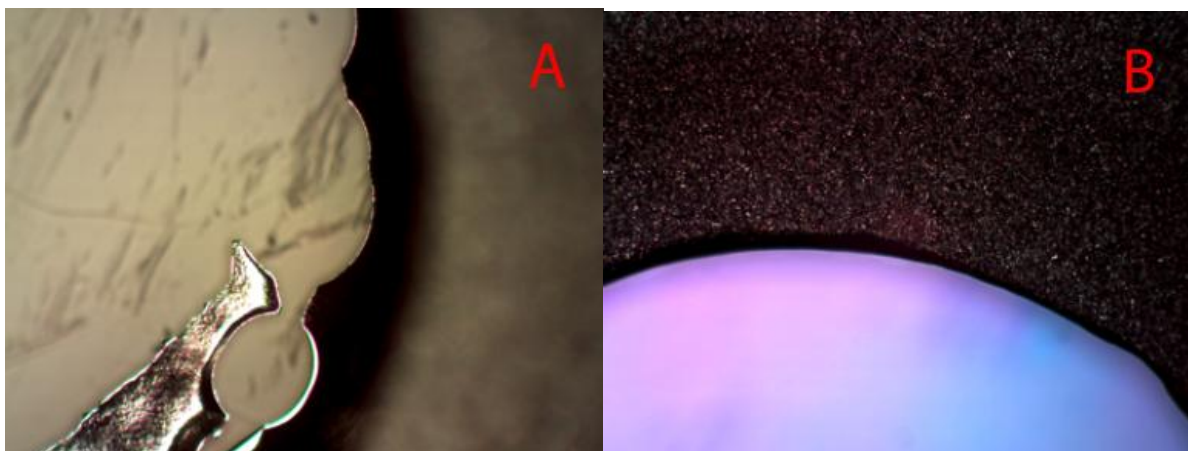


Figure 25: Images taken from the optical microscope of the 60 nm sample (A) and 120 nm sample (B) at 10x optical zoom. For the 60 nm sample, the film is not visible, suggesting the film has shattered, however the silvering does seem to have been successful. The 120 nm sample film is clearly visible, showing a slight blue tint.

In Figure 25, the 120 nm sample labelled B shows the expected difference between the film and the substrate, where the film has a slight blue tint. The 60 nm sample however seems to no longer be visible in the window. The edge of the hole is ragged rather than smooth, suggesting that the film has shattered. Further evidence to the broken film is given by the scratches which can be seen in the hole, which more than likely came from the microscope slide which was placed under the sample to support it. The silvering has worked, however the sample is not longer suitable for secondary electron emission experiments. It is thought the same breaking of the film happened to the 80 nm sample, and that therefore it was the samples becoming loose from the silver dag that caused the film to shatter rather than the silvering process.

The 20 nm, 35 nm and 150 nm samples remained secured to the sample holder. Although the 20 nm and 35 nm films are incredibly delicate, as they did not come loose from the sample stage it was thought that these films may still be intact. As with the 120 nm sample, the 150 nm sample showed a blue tint when held up to the light. It was decided that preliminary experiments would be carried out using the 150 nm sample and the copper plate setup, as the 150 nm film could still be seen in the window, and the 120 nm may have been weakened after coming loose from the silver dag and consequently being replaced onto the sample holder and therefore could be liable to break.

3.2.3.2 Preliminary Data from New Setup

The 150 nm screen was thought to still be intact, so the 150 nm sample was positioned under the electron gun and the Beam Scan program run. After several runs, despite the indistinct quality of the image, the x and y deflection voltages for the beam at 1200 eV were satisfactorily determined. It had previously been found that the x and y coordinates did not stay constant as the primary beam energy changed as they represent deflection voltages, not straight Cartesian coordinates as previously thought. For example, higher primary beam energies needed much higher x and y deflection voltages to move the beam to the same point on the sample as lower beam energies. As the LabView software was written to hold the x and y deflection coordinates, it was decided that these experiments would all be run manually. While far more time consuming, there was a much higher chance of keeping the beam in the same place and producing reliable results.

Two other small alterations were made to the experimental procedure. First, the primary beam current, which was independent of the primary beam energy, was increased from around 2.9 μA to 10 μA . As the current could fluctuate slightly during experiments, the primary beam current for each primary beam energy was recorded. A bias of 40 V was also put on the copper mesh above planar transmission screen: the planar copper plate was used first by itself to ensure that current generated by electrons could be measured, and a bias was applied to help attract the low energy electrons. As the 150 nm film was not expected to start transmitting primary electrons along with secondaries until the primary beam energy reach 4600 eV, a bias on the planar copper plate for the duration of the experiment was not expected to attract a large number, if any, of primary electrons along with the secondaries.

Prior to running the experiment, the electron gun was turned on and the beam aimed far away from the sample and the background current measured, which remained steady at 0.04 μA whenever else it was checked during the experiment. To find the exact position of the hole, the deflection voltages were set to the values decided for a beam energy of 1200 eV, then the x and y values were altered to scan over the area. The current generated from electrons striking the copper plate was monitored as the x and y voltages were changed: the highest current was thought to represent the primary beam striking the centre of the diamond window. The current generated was recorded from the multimeter for each primary beam energy, as was the primary beam current, and therefore the secondary electron yield could be calculated as per Equation 1. The results from the experiment are shown in Figure 26.

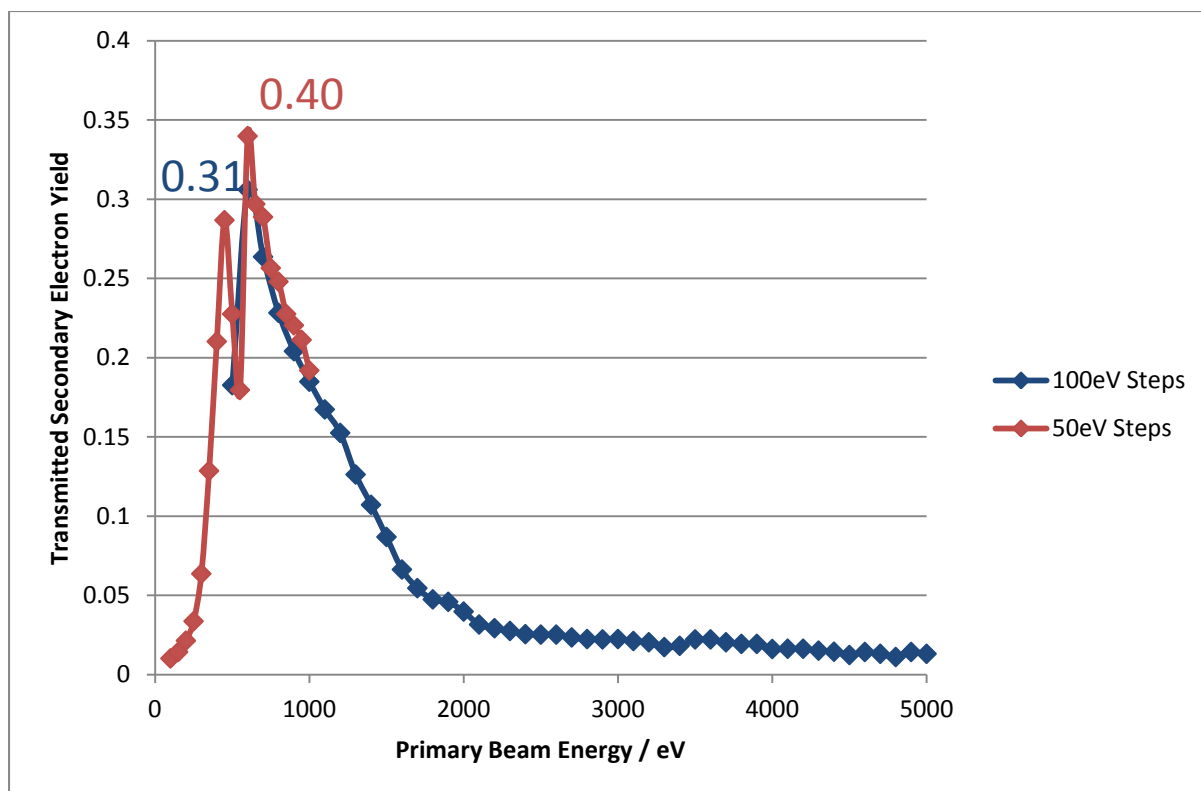


Figure 26: Graph of the change in transmitted secondary electron yield with primary beam energy.

Two experiments were run: one from 500 eV to 5000 eV in steps of 100 eV, and a second from 100 eV to 1000 eV in steps of 50 eV, to check reliability of results and further probe the lower end of the curve.

The change in secondary electron yield with primary beam energy can be seen in Figure 26. For both experiments, the peak in secondary electron yield was at 600 eV, slightly higher than the intensity peak position of 500 eV from the preliminary experiments. After the peak the secondary electron yield started to decrease to a plateau at higher primary beam energies. It would be expected that the secondary electron yield may start to increase from 4600 eV as this was the primary beam energy predicted by CASINO to be the point at which primary electrons started to be transmitted as well. There is no clear increase; all the values of secondary electron yield fluctuate between 0.011 and 0.014 for primary beam electrons between 4600 eV and 5000 eV, which suggests that primary electrons had not yet started to be transmitted. However, Yater et al. did not expect primary electrons to be transmitted through their 150 nm sample until the primary beam energy was over 5000 eV⁷², so perhaps an increase in yield for the planar copper plates would have been seen if the experiment could have been carried out at higher primary beam energies. Furthermore, the data lack the high energy second peak visible for all samples in Figure 22. Therefore the peak may be due to an experimental issue with the phosphor screen; the screen may not have been properly

connected, leading to the screen collecting charge and discharging later on. However, the discharging would be a random process while the second peaks all start to appear around 1500 eV in a systematic pattern. While for the 20 nm sample this may be primary electrons starting to be transmitted through the sample, the primary electrons would not be expected to be transmitted until much higher energies for the thicker samples, as shown in Figure 20.

In Figure 26, the values for secondary electron yield are different for the two experiments carried out: 0.40 for the experiment carried out in primary beam energy steps of 50 eV, and 0.31 for the experiment carried out in 100 eV primary beam energy steps. Furthermore, a smaller peak can be seen at 450 eV with a value of 0.29 for the experiment carried out in 50 eV steps. The second peak is thought to be an issue with a setting on the electron gun called focus. The focus is adjusted to minimise the 'spot size' when the electron beam strikes the sample. The electron gun had been previously calibrated to find the ideal focus for the smallest spot size, and the values from the previous calibration were used during this study. It was decided that the focus would be altered to see the effect of the focus on the secondary electron yield, and the data from the experiment are plotted in Figure 27.

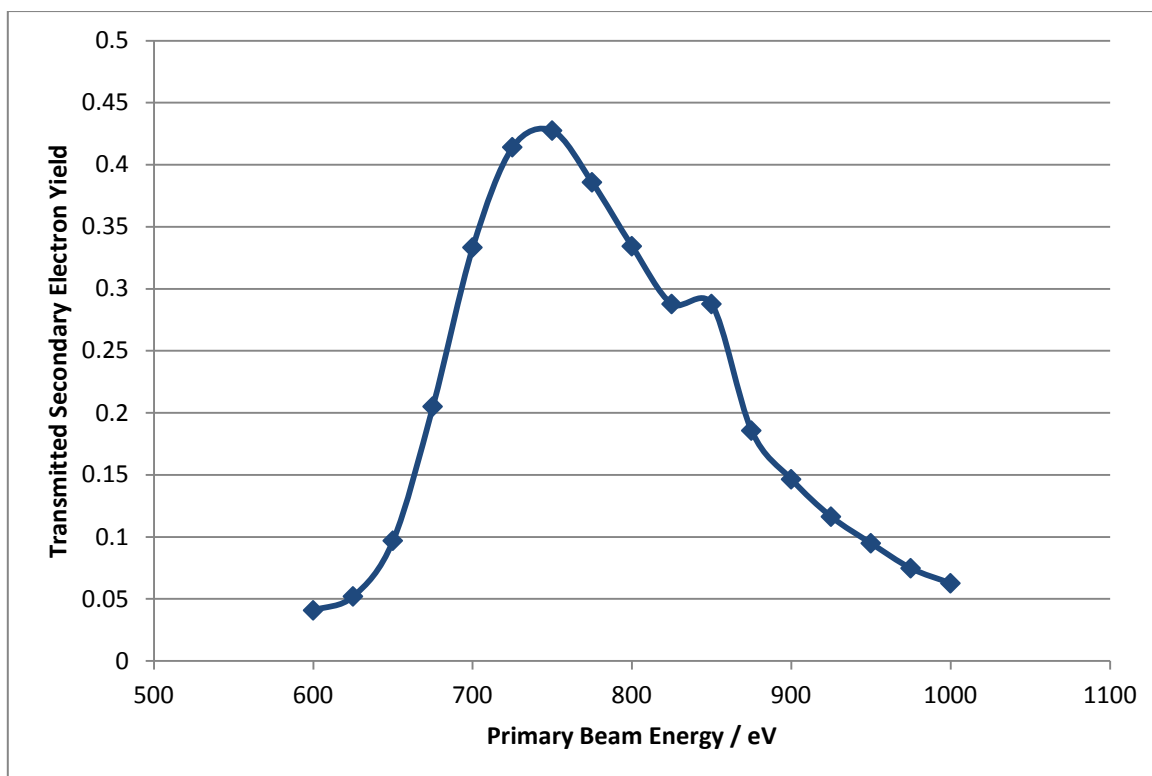


Figure 27: Plot of transmitted secondary electron yield against primary beam energy for adjusted focus results, where the focus was optimised to maximise secondary electron yield. The secondary electron yield has changed from the earlier results, shifting the peak across to 750 eV with a value of 0.43.

Figure 27 shows the new secondary electron yield results for optimised focus. The experiments were carried out between 600 eV and 1000 eV at intervals of 25 eV; 600 eV was the original peak location but as the peak was very sharp rather than the ‘bell-shaped’ curve expected, the region between 600 eV and 1000 eV was chosen for focus alteration to see if in fact the secondary electron yield decreased more uniformly if the focus was changed. Despite 600 eV previously being the location of the 0.41 yield peak, the result shown in Figure 27 is much lower than expected, despite the peak location previously being repeatable. Plotting the data in Figure 27 on the same scale as that in Figure 26 shows that the peak shape is the same but just shifted across for the peak location to stand at 750 eV, and with only a slightly higher yield. The focus was calibrated using the phosphor screens, trying to minimise the spot size on the phosphor screen with the beam striking the phosphor screen directly. The calibration process was harder at lower primary beam energies, and perhaps further investigation into focus would be worthwhile in order to better calibrate the electron gun filament. As only a small section of the diamond can be struck by the primary electron beam, a higher transmission secondary yield would be associated with a small spot size contained in

the entirety of the diamond window. Further work could include repeating the calibration process to check the focus calibration curve.

Comparing the reflection and transmission yields for the 150 nm sample, the reflection peak of 1.42 at 500 eV is higher than that of the transmission yields, which is 0.43 at 750 eV. The higher yield for reflection mode is expected, the secondary electrons have to travel through to the other side of the sample before being emitted while in reflection mode the electrons generated near the sample surface have less distance to travel and more chance of being emitted. However, the potential of transmission secondary electron emission for photomultiplier devices is high: the stacking of several films in a transmission configuration could lead to much higher yields than in reflection mode, due to a cascade effect.

3.3 CASINO 3D Simulations

CASINO 3D simulations were also carried to simulate the secondary electron yields of the samples at different energies. In literature, results are either said to agree with simulations or simulations are used to predict where maximum yield should be and then experiments used to verify but it is rare to find plots of secondary electron yield as a function of primary beam energy. A plot of simulated secondary electron yield as function of primary beam energy has not been found for diamond, only aluminium, where overall the curve has a qualitative shape match between simulation and experiment but experiment has higher yields at lower primary beam energies – there is no real distinction between backscattered and secondary electrons.

The exact work function of these particular samples is unknown so three values used – 5.5 eV (given by software when diamond selected as sample composition), and then 3.9 eV and 2.85 eV which are literature given highest and lowest work functions for hydrogen-terminated diamond⁹². The results for the simulations for the 150 nm sample are given in Figure 28, as both reflection and transmission yields have been calculated for the 150 nm sample. The other graphs can be found in Appendix 8.2. The CASINO software does not make clear the configuration of secondary electron measurement (reflection or transmission), but simulated peaks of above 1 would suggest a reflection configuration.

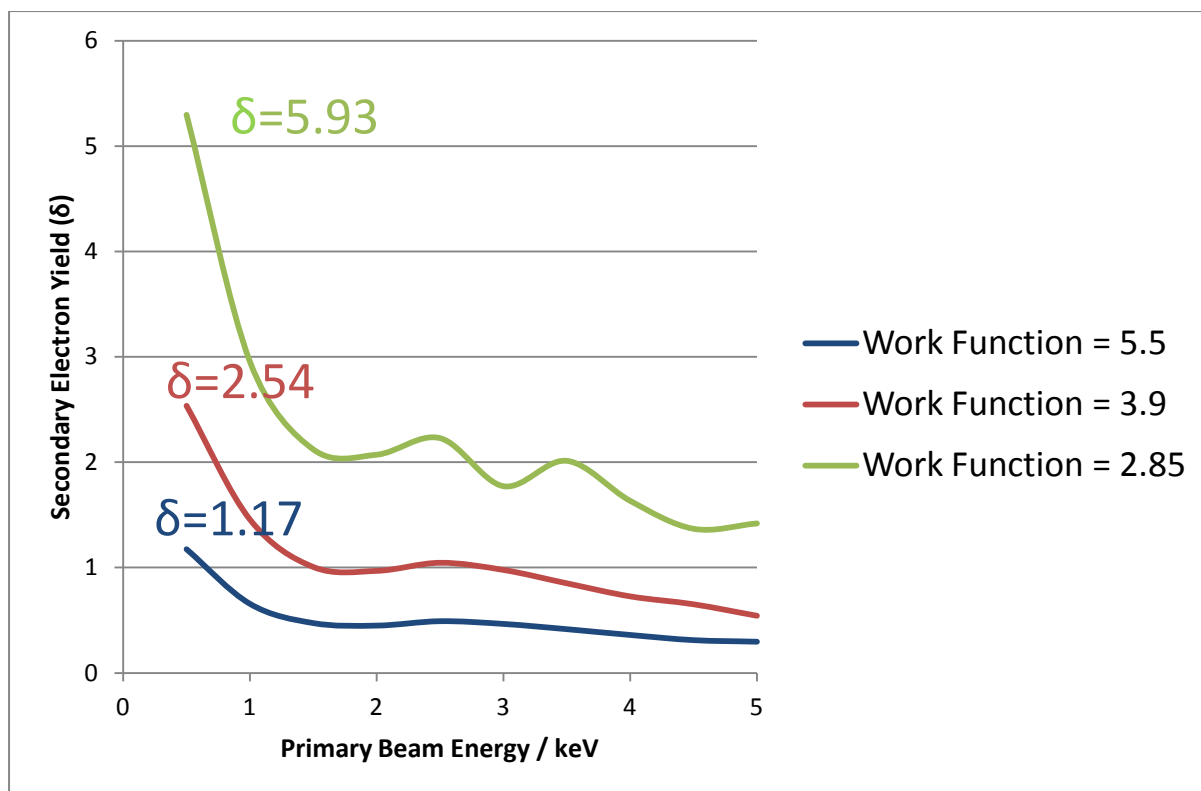


Figure 28: Secondary electron yield curves for the 150 nm thick sample as a function of primary beam energy, for three different work functions. By comparing experimental results to the simulated curves it is possible to estimate the work function of the diamond samples used in the experiments.

In Figure 19, the simulations with lower work functions give higher secondary electron yields – there is a smaller energy barrier for the secondary electrons to overcome to reach vacuum level, which as a negative electron affinity material poses no barrier to electron emission. The shape of the curve most closely matches the reflection yield curve as seen in Figure 19, and the higher yield values suggest that these secondary electron yields correspond to yields measured in a reflection configuration. The work function which is closest to the measured reflection yield of 1.42 is the curve for a 5.5 eV work function. The result is surprising as 5.5 eV was used as a diamond work function only as it was the set value in the software itself, however the work function of bare diamond is given as 5.5 eV⁹² and after repeated exposure of the samples to the electron beam any hydrogen termination would have been destroyed. However, the software simulates perfect samples, taking no account of grain boundaries or other samples imperfections, and also does not account for secondary electrons below 10eV due to software restrictions, so a true secondary electron is defined by the software as having an energy between 10 eV and 50 eV.

Finally, with an estimated work function for the samples of 5.5 eV, which is surprisingly high, the simulated secondary electron curves for all samples with a 5.5 eV work function have been plotted in Figure 29.

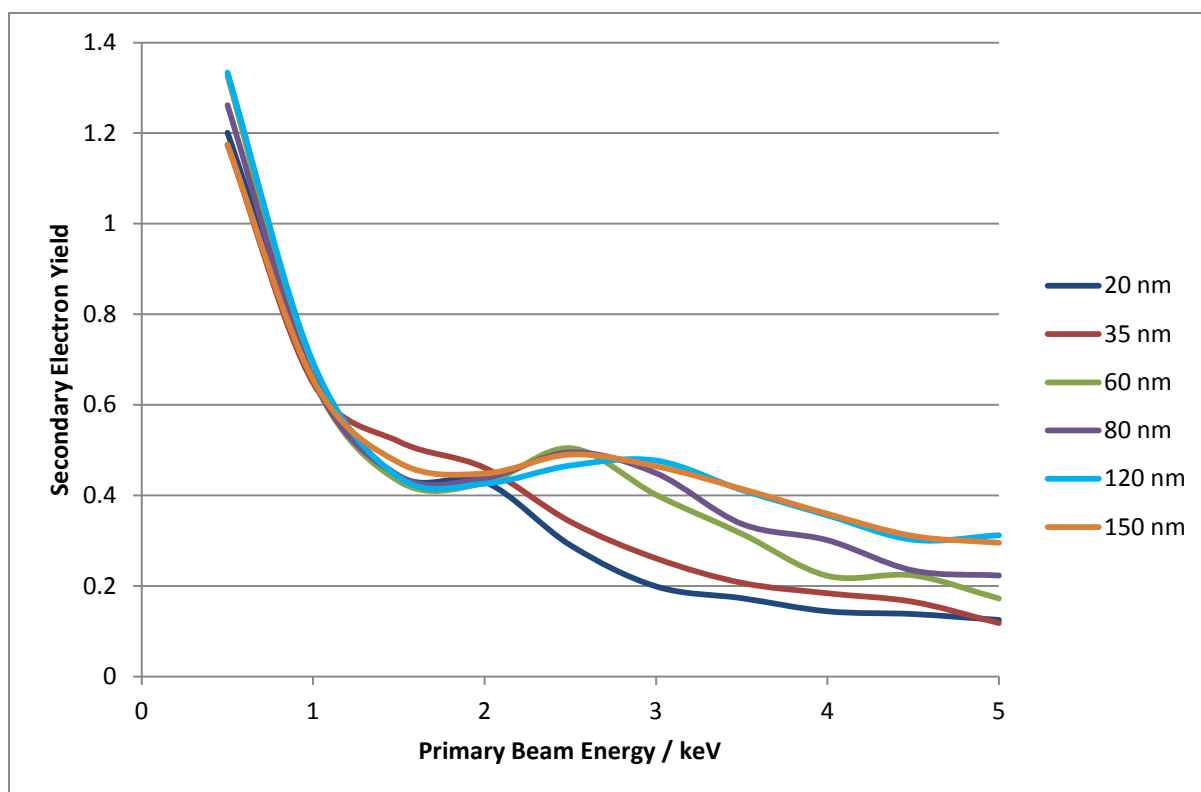


Figure 29: Secondary electron yield curves in reflection mode for all samples at a work function of 5.5 eV. The maximum secondary electron yields vary from 1.17 for the 150 nm sample and 1.33 for the 60 nm and 120 nm samples.

Figure 29 shows the secondary electron yield curves for all samples with a work function of 5.5 eV. Even with different sample thicknesses, the 0.5-1.0 keV region of the curve shows remarkably similar behaviour, with a standard deviation of 0.07 between the results. While the curves deviate from one another on the latter part of the curve, as Monte Carlo simulation is a random number generator-based simulation, the curves could in fact be identical, allowing for fluctuations in the random nature of the simulation. While the reflection curves in Figure 19 show a general decrease in yield with increases in sample thickness, at higher energies (above 4 keV) the simulations appear to predict an increase in secondary electron yield with sample thickness.

While the possibility of simulating secondary electron yields is useful for comparison of experimental results, particularly if the software could be tailored for an exact film composition for which literature data may not be available, the CASINO software is limited. It can predict the overall shape

expected of secondary electron curves, but perhaps provides a better building block from which a more advanced code could be developed.

4 Conclusions

The emission of 'true' secondary electrons, defined as those with energies of less than 50 eV, takes place when electrons within a material are excited by those in a primary electron beam, and consequently these excited electrons are able to escape from the surface of a material, such as a diamond film. In the literature, the secondary electron yield from diamond films has been measured extensively in reflection mode, where secondary electrons are emitted from the incidence point, but much less so in transmission mode, where much thinner films are needed to ensure the secondary electrons travel to the other side of the film. While some simulation work on secondary electron emission in transmission mode has been carried out, there is usually little distinction between the true secondary electrons emitted, and those that have been backscattered. Furthermore, comparisons between simulation and experiment for diamond are few in number, and the literature focuses more on the analysis methods used in simulation rather than on the simulation results themselves.

A custom-built setup has been used to measure secondary electron emission in reflection mode and transmission mode under high vacuum. The setup currently makes use of calibrated phosphor screens for the reflection measurements, where the intensity of the light generated upon incident electrons is measured, and copper plates for the transmission measurements, where the current generated by the incident electrons is measured. Six diamond film samples of varying thickness were tested in both reflection and transmission mode, and simulation work carried out to predict the primary beam energy needed for primary electron transmission and the theoretical secondary electron yield.

For the reflection secondary electron yields, measured using the phosphor screens, the highest yield was found to be for the thinnest sample, 20 nm, with a value of 2.90. A slight dependence of secondary electron emission yield on film thickness could be seen, however the thickest film of 150 nm had a higher yield of 1.42, almost double that of the 80 nm film.

In transmission experiments, all the films were only tested using the transmission phosphor screens; however the setup was later altered to overcome some problems with calibration, as the transmission phosphor screen data could not be scaled as the reflection data were. Using the copper

plates, a transmission yield of 0.43 at 750 eV was found for the 150 nm sample, using current measurements rather than intensities from the phosphor screen to calculate the yield. The transmission yield is much lower than the reflection yield, which would be expected, but also considerably lower than Yater et al.'s 150 nm film, which had a yield of 5⁷². However, Yater et al.'s boron-doped films are expected to have higher yields than the undoped samples used in this study, as the boron provides a higher degree of electron conductivity not seen in undoped samples.

Finally, Monte Carlo based programs known as CASINO 2D and 3D have been used to make predictions about the experiments presented here. CASINO 2D has been used to predict the primary beam energy at which primary electrons may be transmitted through the sample, while CASINO 3D has been used to simulate secondary electron yield curves for all the samples, with different work functions. For transmission, it was predicted that a primary beam energy of at least 4600 eV would be needed for the 150 nm sample for primary electrons to be emitted from the transmission surface, which is much higher than the 750 eV where the secondary electron peak was measured. CASINO 3D predicted that samples of different thicknesses would give similar secondary electron yields in reflection mode provided the work function of the sample was the same. CASINO has no function for doping, termination or surface morphology, the inclusion of which would better model the diamond films grown using CVD techniques; however the CASINO code could be further investigated to see if these properties could be included into the simulations.

5 Future Work

There is great scope for future work with the project, particularly once the system is fully set up. First, it may be best to replace the samples: as previously explained, at least two of the films were thought to have shattered during experiments. It may be worthwhile looking at new ways of fixing the samples to the sample holder as well. The silver dag used helps the conductivity and helps to prevent some surface charging; however the strength of the adhesive means that removing the samples more likely than not causes the diamond films to shatter. Particularly for reflection experiments, it is important that the sample is stuck film-side down so that the only diamond exposed to the primary electron beam is the window. If the sample was stuck silicon-side down, the entire diamond film would be exposed which would not be ideal due to some of the positioning issues with the primary beam, although a comparison between secondary electron emission in reflection mode of the diamond window and the diamond film on the sample would no doubt be an interesting comparison. To keep the current film configuration, a conductive silicon support could be

fixed along the edges of the diamond film which could then be secured to the sample holder with the silver dag. There may still be some damage done to the films while removing the supports from the sample holder; however the damage may be a lot less than currently.

Once a new set of sample has been acquired, a full set of experiments needs to be completed in transmission mode for the current setup, with only the planar transmission screen directly below the samples measuring transmitted current. The next step would be to turn on the mesh bias voltage on the second, angled screen. It may first be necessary to alter the bias voltage to ensure only true secondary electrons are attracted to the second transmission screen and measured. A starting voltage would be 50 V, and from there the voltage could be raised or lowered depending on the measured current, and whether or not 50 V attracts no electrons or a high proportion of electrons which may include high energy primaries.

The final step in the setup of the secondary electron setup would be to remove the arm supporting all the screens and add a third transmission screen, also at 45° to the planar transmission screen, and a corresponding mesh over the top which could be biased. The third screen would be a phosphor screen, the same as the reflection screen, and would need a photomultiplier tube for measuring the intensity of the light generated by the electrons striking the surface. The proposed final setup of the screens inside the vacuum chamber is shown in Figure 30.

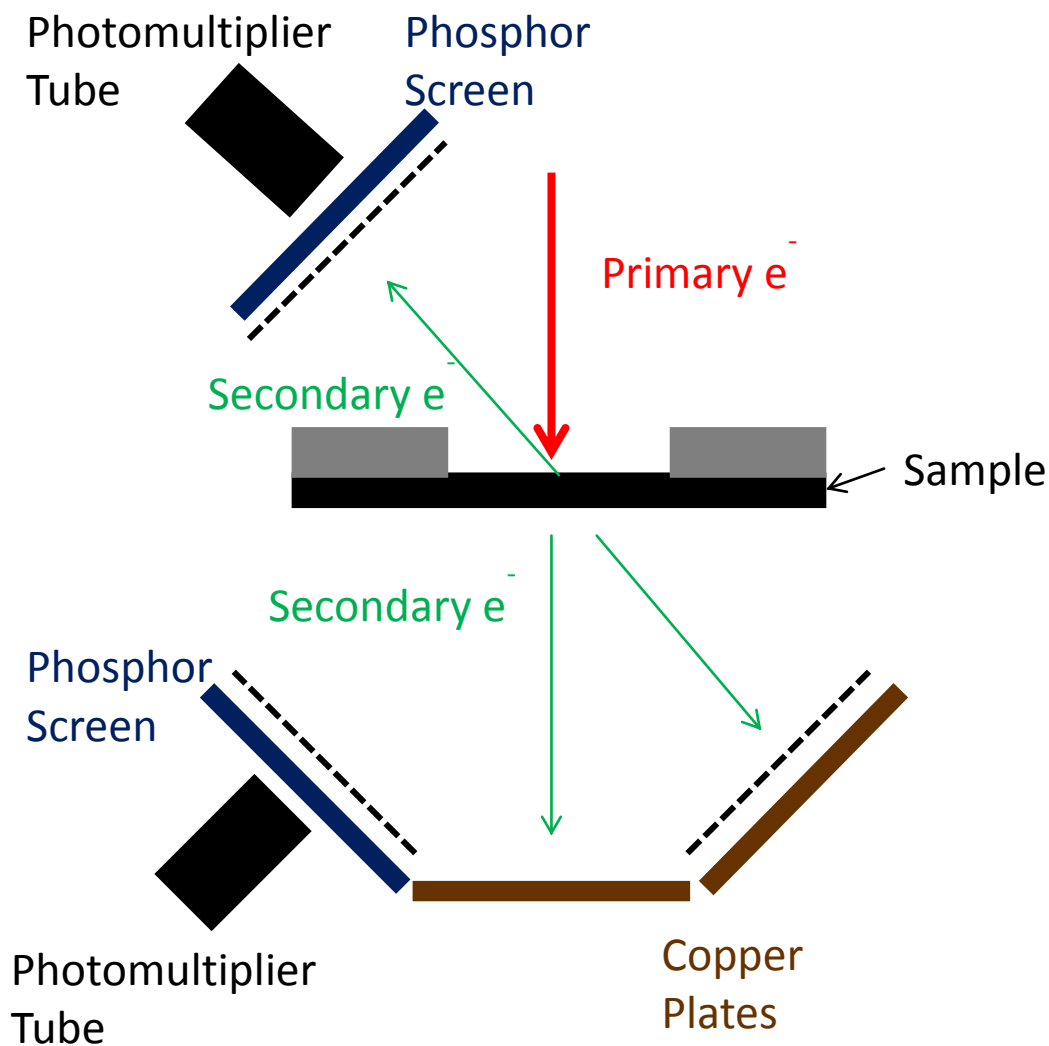


Figure 30: Diagram showing the proposed arrangement of screens inside the secondary setup, where the dashed lines represent the copper meshes. The transmission copper plates could be connected up to a multimeter which could be read in tandem with the phosphor screen intensity measurements from the photomultiplier tube to provide a calibration for the transmission setup, thus setting up the system to take all secondary electron measurements using phosphor screens.

The proposed configuration in Figure 30 allow secondary electron measurements in transmission mode using the phosphor screen, where the intensities could be calibrated against the current measured on the angled copper plate. The two experiments would not be able to be run concurrently: first the secondary electron measurements would need to be run with the copper plates measuring current. The bias voltage would then be removed from the copper plate mesh and applied to the phosphor screen mesh. The intensity signal generated by the phosphor screen should exactly match the current measured by the copper screen, so by calibrating the intensity signal against the current, a secondary electron yield for transmission using the phosphor screen could

then be calculated, allowing secondary electron measurements to be made purely using the phosphor screens in both reflection and transmission mode. Once the setup is fully calibrated, a wider variety of films can be tested in both reflection and transmission mode. Starting with a boron-doped sample would be recommended, to see if results from Yater et al. on the thinnest films found in literature so far are comparable to results from the custom-built setup⁷². Further investigations could include:

1. Effect of the level of boron doping on transmission secondary electron yield, and whether the optimum boron concentration for optimum secondary electron yield differs between films of different thicknesses
2. Effect of different surface terminations, such as hydrogen termination and caesium termination to see if caesium termination gives far higher yields as in reflection mode, and whether both the higher quality emission surface and the diamond surface upon which the primary electron beam is incident need to be treated for a particular surface termination for optimum secondary electron yields
3. Effect of surface morphology on transmission secondary electron yield, and whether the results are comparable to the effects of surface morphology in reflection mode
4. Effect of the substrate the diamond is grown on, and whether the technique used to remove the hole in the substrate affects the diamond surface enough to affect the secondary electron yield, and therefore whether or not free-standing films are preferable

Further work could also be done with the simulation work. CASINO is by far the best free-to-use Monte Carlo simulation available; however it does have considerable drawbacks. One advantage of CASINO is that, providing the origin of the source code is acknowledged, further alterations can be made to the code itself⁹³. CASINO is currently limited by its inability to tell between transmitted primary electron and true secondary electrons emitted in transmission mode, issues with surface terminations (upon setting hydrogen as the surface of the sample for example, the program no longer runs), and the generation of perfect lattices in which dopants, grain boundaries and other impurities cannot be included. Investigation into exactly how the CASINO program works could allow modification of the codes and calculations used to accommodate hydrogen surface termination and possible random allocation of dopant species within the uniform carbon lattice. By including more variables such as termination, doping and surface morphology into the code, simulation which closer match experimental conditions can be run, hopefully leading to more accurate simulation results with respect to the experimental data.

6 Acknowledgements

I would like to thank my supervisor Professor Paul May for offering me this project and for his help and guidance throughout my project. I would also like to thank my second assessor, Dr Neil Fox, for his advice and suggestions, even if unfortunately I didn't have the chance to implement half of them due to time restraints. Special thanks to Dr James Smith and Jan Harwood for their unerring patience and help with a setup that refused to cooperate; without their help I would undoubtedly still be sat in the diamond lab wondering what had gone wrong.

7 References

1. Mittemeijer, E.J. Fundamentals of materials science : the microstructure-property relationship using metals as model systems (Springer, Heidelberg ; London, 2010).
2. Pan, L.S. & Kania, D.R. Diamond : electronic properties and applications (Kluwer Academic, Boston ; London, 1995).
3. Nazare, M.H. & Neves, A.J. Properties, growth and applications of diamond (Institution of Electrical Engineers, London, 2001).
4. Yin, M.T. & Cohen, M.L. Ground-state properties of diamond. *Physical Review B* **24**, 6121-6124 (1981).
5. Sung, J.C. & Lin, J. Diamond nanotechnology : syntheses and applications (Pan Stanford ; London : World Scientific [distributor], Singapore, 2010).
6. Prelas, M.A., Popovici, G. & Bigelow, L.K. Handbook of industrial diamonds and diamond films (Marcel Dekker, New York, 1998).
7. Ashfold, M.N.R., May, P.W., Rego, C.A. & Everitt, N.M. Thin Film Diamond by Chemical Vapour Deposition Methods. *Chemical Society Reviews* **23**, 21-30 (1994).
8. Spear, K.E. & Dismukes, J.P. Synthetic diamond : emerging CVD science and technology (Wiley & Sons, New York ; Chichester, 1994).
9. Bundy, F.P.H., H.T.Strong, H.M.Wentorf Jr, R.H. Man-Made Diamonds. *Nature* **176**, 51-55 (1955).
10. Asmussin, J., Asmussen, J. & Reinhard, D.K. Diamond films handbook (Marcel Dekker, New York, 2002).
11. Akaishi, M., Kanda, H. & Yamaoka, S. Synthesis of Diamond from Graphite-Carbonates Systems under very high Temperature and Pressure *Journal of Crystal Growth* **104**, 578–581 (1990).
12. Caveney, R.J. Limits to quality and size of diamond and cubic boron nitride synthesized under high pressure, high temperature conditions *Materials Science and Engineering B* **11**, 197-205 (1992).
13. Bachmann, P.K., Leers, D. & Lydtin, H. Towards a general concept of diamond chemical vapour deposition. *Diamond & Related Materials* **1**, 1-12 (1992).
14. Haubner, R. & Lux, B. Diamond growth by hot-filament chemical vapor deposition: state of the art *Diamond and Related Materials* **2**, 1277–1294 (1993).
15. Chu, C.J., D'Evelyn, M.P., Hauge, R.H. & Margrave, J.L. Mechanism of diamond film growth by hot-filament CVD: Carbon-13 studies *Journal of Materials Research* **5**, 2405-2413 (1990).

16. Celii, F.G. & Butler, J.E. Diamond Chemical Vapor Deposition. *Annual Review of Physical Chemistry* **42**, 643-684 (1991).
17. Vaz, R.M.A. in School of Chemistry (University of Bristol, 2013).
18. May, P.W. Diamond thin films: a 21st-century material. *Philosophical Transactions of the Royal Society A* **358**, 473-495 (2000).
19. Bohr, S., Haubner, R. & Lux, B. Influence of nitrogen additions on hot filament chemical vapor deposition of diamond. *Applied Physics Letters* **68**, 1075-1077 (1996).
20. Butler, J.E., Woodin, R.L., Brown, L.M. & Fallon, P. Thin Film Diamond Growth Mechanisms [and Comment]. *Philosophical Transactions of the Royal Society A* **342**, 209-224 (1993).
21. Skokov, S., Carmer, C.S., Weiner, B. & Frenklach, M. Reconstruction of (100) diamond surfaces using molecular dynamics with combined quantum and empirical forces. *Physical Review B* **49** (1994).
22. Yan, C., Vohra, Y.K., Mao, H. & Hemley, R.J. Very high growth rate chemical vapor deposition of single-crystal diamond *PNAS* **99**, 12523–12525 (2002).
23. Williams, O.A., Daenena, M., D'Haen, J., Haenen, K., Maes, J., Moshchalkov, V.V. Nesiádek, M. & Gruen, D.M. Comparison of the growth and properties of ultrananocrystalline diamond and nanocrystalline diamond *Diamond and Related Materials* **15**, 654–658 (2006).
24. Reinhard, D.K., Grotjohn, T.A., Becker, M., Yaran, M.K., Schuelke, T. & Asmussen, J. Fabrication and properties of ultranano, nano, and microcrystalline diamond membranes and sheets. *Journal of Vacuum Science and Technology B* **22**, 2811-2817 (2004).
25. Jeedigunta, S. in Department of Electrical Engineering (University of South Florida, Tampa, FL, USA, 2008).
26. Diederich, L., Küttel, O.M., Ruffieux, P., Pillo, T., Aebi, P. & Schlapbach, L. Photoelectron emission from nitrogen- and boron-doped diamond (100) surfaces. *Surface Science* **417**, 41-52 (1998).
27. Diederich, L., Küttel, O.M., Aebi, P. & Schlapbach, L. Electron affinity and work function of differently oriented and doped diamond surfaces determined by photoelectron spectroscopy. *Surface Science* **418**, 219–239 (1998).
28. Fujimori, N., Imai, T. & Doi, A. Characterization of conducting diamond films *Vacuum* **36**, 99-102 (1986).
29. Trucchi, D.M., Scilletta, C., Cappelli, E., Merli, P.G., Zoffoli, S., Mattei, G. & Ascarelli, P. Optimization of the performance of CVD diamond electron multipliers. *Diamond & Related Materials* **15**, 827–832 (2006).

30. Ternyak, O., Michaelson, S., Akhvlediani, R. & Hoffman, A. Enhancement of electron emission from near-coalescent nanometer thick continuous diamond films *Diamond & Related Materials* **15**, 850 – 853 (2006).
31. Bruining, H. Physics and Applications of Secondary Electron Emission (McGraw-Hill Book Co.: New York; Pergamon Press: London; printed in Great Britain, 1954).
32. Tipler, P.A. & Mosca, G. Physics for scientists and engineers : with modern physics (Palgrave Macmillan, Basingstoke, 2008).
33. Sawyer, L., Grubb, D. & Meyers, G.F. Polymer Microscopy (Springer, New York, USA, 2008).
34. Gucsik, A. Cathodoluminescence and its Application in the Planetary Sciences (Springer, Berlin, 2009).
35. Archard, G. Back Scattering of Electrons *Journal of Applied Physics* **32**, 1505-1509 (1961).
36. McNaught, A.D. & Wilkinson, A. (eds.) IUPAC. Compendium of Chemical Terminology, 2nd ed. (the "Gold Book") (Blackwell Scientific Oxford, 1997).
37. Scholtz, J., Dijkamp, D. & Schmitz, R. Secondary electron emission properties. *Philips Journal of Research* **50**, 375-389 (1996).
38. Walker, C., El-Gomati, M., Assa'd, A. & Zadrazil, M. The Secondary Electron Emission Yield for 24 Solid Elements Excited by Primary Electrons in the Range 250-5000 eV: A Theory/Experiment Comparison. *Scanning* **30**, 365-380 (2008).
39. Bell, D.C. & Erdman, N. Low voltage electron microscopy : principles and applications (ed. Brooks, S.) (John Wiley & Son, Chichester, UK, 2013).
40. Wolff, P. Theory of Secondary Electron Cascade in Metals. *Physical Review* **95**, 56-66 (1954).
41. Seah, M. Slow Electron Scattering from Metals: 1. Emission of True Secondary Electrons. *Surface Science* **17**, 132-160 (1969).
42. Simons, R. & Williams, B. Secondary-Electron Emission. *IEEE Transactions on Nuclear Science* **15**, 167-170 (1968).
43. Shih, A., Yater, J., Pehrsson, P., Butler, J., Hor, C. & Abrams, R. Secondary electron emission from diamond surfaces. *Journal of Applied Physics* **82**, 1860-1867 (1997).
44. Marton, L. Advances in Electronics (Academic Press Inc., New York, 1948).
45. Dionne, G. Origin of secondary electron emission yield curve parameters. *Journal of Applied Physics* **46**, 3347-3351 (1975).
46. Vaughan, J. A new formula for secondary emission yield. *IEEE Transactions on Electron Devices* **36**, 1963-1967 (1989).
47. Shih, A., Yater, J., Hor, C. & Abrams, R. Secondary electron emission studies. *Applied Surface Science* **111**, 251-258 (1997).

48. Kittel, C. Introduction to solid state physics (John Wiley, Hoboken, N.J., 2005).
49. Van der Weide, J., Zhang, Z., Baumann, P.K., Wensell, M.G., Bernholc, J. & Nemanich, R.J. Negative-electron-affinity effects on the diamond (100) surface. *Physical Review B* **50**, 5803-5806 (1994).
50. Cui, J., Ristein, J. & Ley, L. Electron affinity of the bare and hydrogen covered single crystal diamond (111) surface. *Physical Review Letters* **81**, 429-432 (1998).
51. Himpsel, F., Knapp, J., Van Vechten, J. & Eastman, D. Quantum photoyield of diamond(111)—A stable negative-affinity emitter. *Physical Review B* **20**, 624-627 (1979).
52. Jewett, J.W. & Serway, R.A. Physics for scientists and engineers with modern physics (Brooks/Cole, [Pacific Grove, Calif.?], 2010).
53. Lye, R. & Dekker, A. Theory of Secondary Emission. *Physical Review* **107**, 977-981 (1957).
54. Eyges, L. Straggling of Electrons Near the Critical Energy. *Physical Review* **76**, 262-269 (1949).
55. Lin, Y. & Joy, D. A new examination of secondary electron yield data. *Surface and Interface Analysis* **37**, 895-900 (2005).
56. Demers, H., Demers, H., Poirier-Demers, N., Couture, A.R. Joly, D., Guilmain, M., de Jonge, N. & Drouin, D. Three-Dimensional Electron Microscopy Simulation with the CASINO Monte Carlo Software. *Scanning* **33**, 135-146 (2011).
57. Tissue, B.M. Basics of Analytical Chemistry and Chemical Equilibria (John Wiley & Sons, New Jersey, 2013).
58. Lyman, C.E. Scanning electron microscopy, X-ray microanalysis, and analytical electron microscopy : a laboratory workbook (Plenum, New York ; London, 1990).
59. Kawata, J., Ohya, K. & Nishimura, K. Simulation of secondary electron emission from rough surfaces. *Journal of Nuclear Materials* **220**, 997-1000 (1995).
60. Yater, J., Shih, A. & Abrams, R. Electronic properties of diamond for high-power device applications. *Solid-State Electronics* **42**, 2225-2232 (1998).
61. Yater, J., Shih, A., Butler, J. & Pehrsson, P. Transmission of low-energy electrons in boron-doped nanocrystalline diamond films. *Journal of Applied Physics* **93**, 3082-3089 (2003).
62. Yater, J., Shaw, J.L., Jensen, K.L., Feygelson, T., Myers, R.E., Pate, B.B. & Butler, J.E. Secondary electron amplification using single-crystal CVD diamond film. *Diamond and Related Materials* **20**, 798-802 (2011).
63. Wang, J., Wang, P., Belhaj, M. & Velez, J. Modeling Facility Effects on Secondary Electron Emission Experiment. *Ieee Transactions on Plasma Science* **40**, 2773-2780 (2012).
64. Shih, A. & Hor, C. Secondary Emission Properties as a Function of the Electron Incidence Angle *IEEE Transactions on Electron Devices* **40**, 824-829 (1993).

65. May, P.W., Stone, J.C., Ashfold, M.N.R., Hallam, K.R., Wang, W.N. & Fox, N.A. The effect of diamond surface termination species upon field emission properties *Diamond and Related Materials* **7**, 671-676 (1998).
66. Yater, J.E., Shih, A. & Abrams, R. Electron transport and emission properties of diamond. *Journal of Vacuum Science and Technology A* **16**, 913-918 (1998).
67. Ascarelli, P., Cappelli, E., Pinzari, F., Rossi, M.C., Salvatori, S., Merli, P.G. & Migliori, A. Secondary electron emission from diamond: Physical modeling and application to scanning electron microscopy. *Journal of Applied Physics* **89**, 689-696 (2001).
68. Mearini, G.T., Mearini, G.T., Krainsky, I.L., Wang, Y.X., Dayton Jr., D.A., Ramesham, R. & Rose, M.F. Fabrication of an electron multiplier utilizing diamond films *Thin Solid Films* **253**, 151-156 (1994).
69. Bekker, T.L., ;Dayton Jr., J.A., Gilmour Jr., A.S., Krainsky, I.L., Rose, M.F., Rameshan, R., File, D. & Mearini, G. in *Electron Devices Meeting 949-952 (Technical Digest, International, San Francisco, CA, USA, 1992)*.
70. Chang, X. et al. in *Pres. Particle Accelerator Conf. (Knoxville, 2005)*.
71. Yater, J., Shih, A., Butler, J. & Pehrsson, P. Electron transmission studies of diamond films. *Applied Surface Science* **191**, 52-60 (2002).
72. Yater, J., Shih, A., Butler, J. & Pehrsson, P. Electron transport mechanisms in thin boron-doped diamond films. *Journal of Applied Physics* **96**, 446-453 (2004).
73. Dvorkin, V., Dzbanovsky, N.N., Suetin, N.V., Poltoratsky, E.A., Rychkov, G.S., Il'ichev, E.A., & Gavrilov, SA Secondary electron emission from CVD diamond films. *Diamond and Related Materials* **12**, 2208-2218 (2003).
74. Dimitrov, D. et al. Multiscale three-dimensional simulations of charge gain and transport in diamond. *Journal of Applied Physics* **108** (2010).
75. Wang, E.D, Ben-Zvi, I., Rao, T., Dimitrov, D.A., Chang, X.Y., Wu, Q. & Xin, T.M. Secondary-electron emission from hydrogen-terminated diamond: Experiments and model. *Physical Review Special Topics-Accelerators and Beams* **14** (2011).
76. Dimitrov, D., Wang, E., Smedley, J., Ben-Zvi, I. & Rao, T. in *Vacuum Electronics Conference (IVEC), 2013 IEEE 14th International 21-23 May 2013 (IEEE, Paris, France, 2013)*.
77. Koshikawa, T. & Shimizu, R. Secondary electron and backscattering measurements for polycrystalline copper with aspherical retarding-field analyser. *Journal of Physics D: Applied Physics* **6**, 1369-1380 (1973).
78. Insepov, Z., Ivanov, V. & Frisch, H. Comparison of candidate secondary electron emission materials. *Nuclear Instruments and Methods in Physics Research B* **268**, 3315–3320 (2010).

79. Garth, J.C. in *The Monte Carlo Method: Versatility Unbounded In A Dynamic Computing World* (American Nuclear Society, Chattanooga, Tennessee, 2005).
80. Hamme, F., Becker, U. & Hammes, P. in *International Computational Accelerator Physics* (Chamonix, France, 2006).
81. Ritchie, N. A new Monte Carlo application for complex sample geometries. *Surface and Interface Analysis* **37**, 1006-1011 (2005).
82. Villarrubia, J., Ritchie, N., Lowney, J. & Archie, C. Monte Carlo modeling of secondary electron imaging in three dimensions - art. no. 65180K. *Metrology, Inspection, and Process Control for Microlithography XXI, Pts 1-3* **6518**, K5180-K5180 (2007).
83. Praver, S., Rubanov, S., Hearne, S., Jamieson, D. & Kalish, R. Spatial extent of band bending in diamond due to ion impact as measured by secondary electron emission: Experiment and theory. *Physical Review B* **73** (2006).
84. Morozov, A. et al. Transmission of similar to 10 keV electron beams through thin ceramic foils: Measurements and Monte Carlo simulations of electron energy distribution functions. *European Physical Journal D* **48**, 383-388 (2008).
85. Agostinelli, S. et al. GEANT4-a simulation toolkit. *Nuclear Instruments & Methods in Physics Research Section a-Accelerators Spectrometers Detectors and Associated Equipment* **506**, 250-303 (2003).
86. Allison, J. et al. Geant4 developments and applications. *Ieee Transactions on Nuclear Science* **53**, 270-278 (2006).
87. Morozov, A., Krucken, R., Ulrich, A. & Wieser, J. Spatial distribution of fluorescent light emitted from neon and nitrogen excited by low energy electron beams. *Journal of Applied Physics* **100** (2006).
88. Drouin, D., Couture, A.R., Joly, D., Tastet, X., Aimez, V. & Gauvin, R. CASINO V2.42 - A fast and easy-to-use modeling tool for scanning electron microscopy and microanalysis users. *Scanning* **29**, 92-101 (2007).
89. Assa'd, A. & El Gomati, M. Backscattering Coefficients for Low Energy Electrons. *Scanning Microscopy* **12**, 185-192 (1998).
90. Furman, M.A. & Tivi, M.F.P. Simulation of Secondary Electron Emission Based on a Phenomenological Probabilistic Model *Phys. Rev. ST Accel. Beams* **5**, 124404 (2002).
91. Echlin, P. *Handbook of Sample Preparation for Scanning Electron Microscopy and X-Ray Microanalysis* (Springer, New York, 2011).
92. O'Donnell, K.M., Martin, T.L., Fox, N.A. & Cherns, D. Ab initio investigation of lithium on the diamond C(100) surface. *Physical Review B* **82**, 115303 (2010).

93. Joly, D., Poirier-Demers, N. & Demers, H. Casino 3.2 User Manual. *Universite de Sherbrooke User Manual* (2011).

8 Appendix

8.1 Glossary of Terms

δ	Secondary Electron Yield (SEY)
I_t	Total emitted electron current
I_0	Primary electron current
E_0	Primary electron energy
E_I, E_{II}	Electron energy when SEY is 1
E_m	Electron energy for $\delta = \delta_m$
E_v	Valence band energy
E_c	Conduction band energy
χ	Electron affinity
E_{vac}	Vacuum level
ϕ	Work function
E_F	Fermi level
δ_m	Maximum SEY
z_m	Value of z to maximise the $g_n(z)$ function
E_i	Impact Energy
d	Membrane thickness
B	Probability of an electron escaping the surface
E_{gap}	Bandgap energy
L	Carrier diffusion length
z	Distance from the surface of the sample
G_t	Transmission gain

$E_f(t)$	Time-dependent internal field
a, b, c	Fitting parameters
$S_{background}$	Background intensity signal
S_{sample}	Intensity signal from sample
S_{copper}	Intensity signal from copper sample, used as reference
$\delta_{copper}(E_x)$	Correction factor used in analysis of reflection yield data

8.2 CASINO 3D Simulation Plots

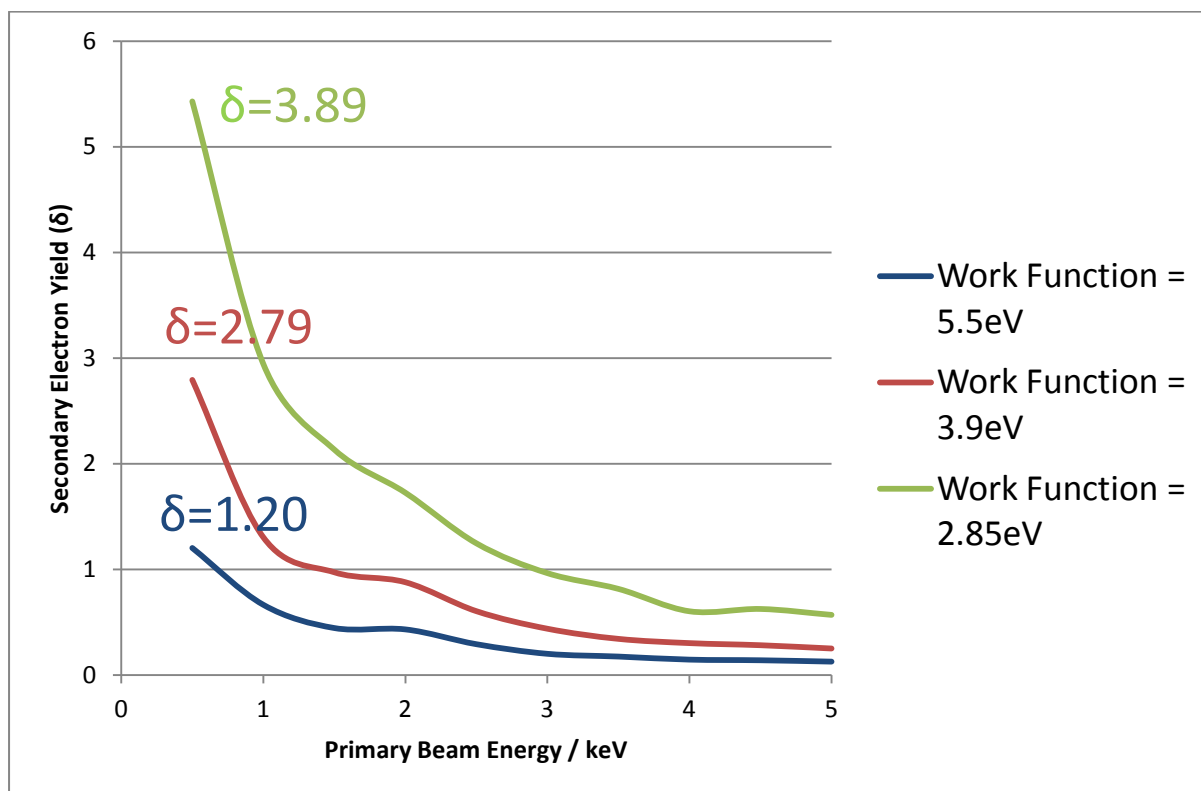


Figure 31: Simulated secondary electron yield curves for the 20 nm sample at a selection of different work functions.

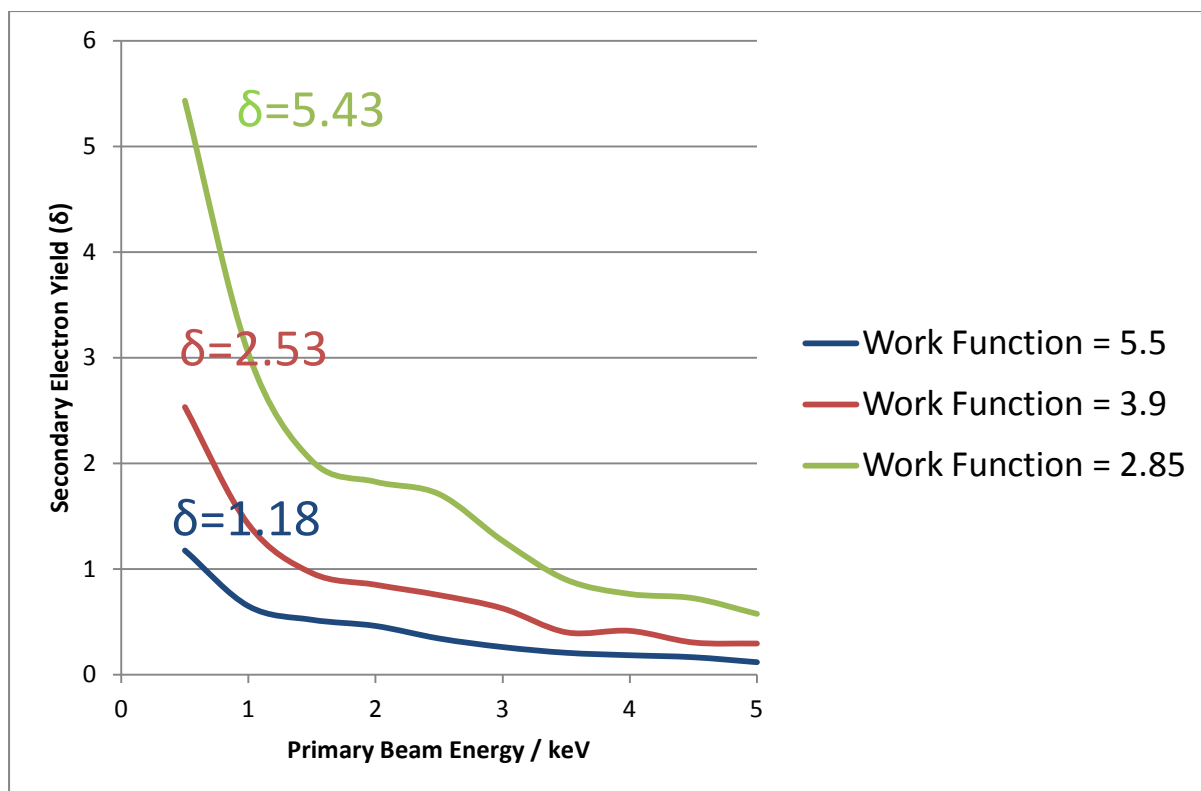


Figure 32: Secondary electron yield as a function of primary beam energy for a simulated 35 nm sample with a variety of different work functions.

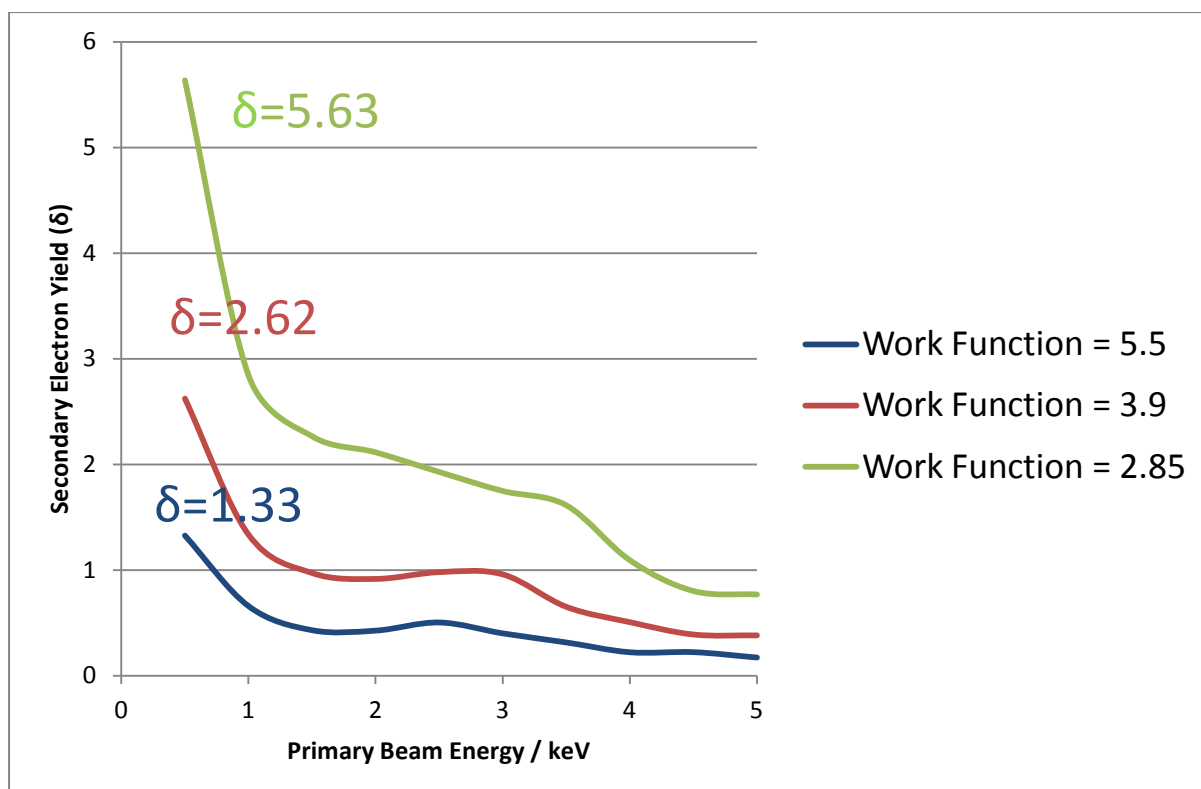


Figure 33: Simulated secondary electron yield curves for a 60 nm sample at several work functions.

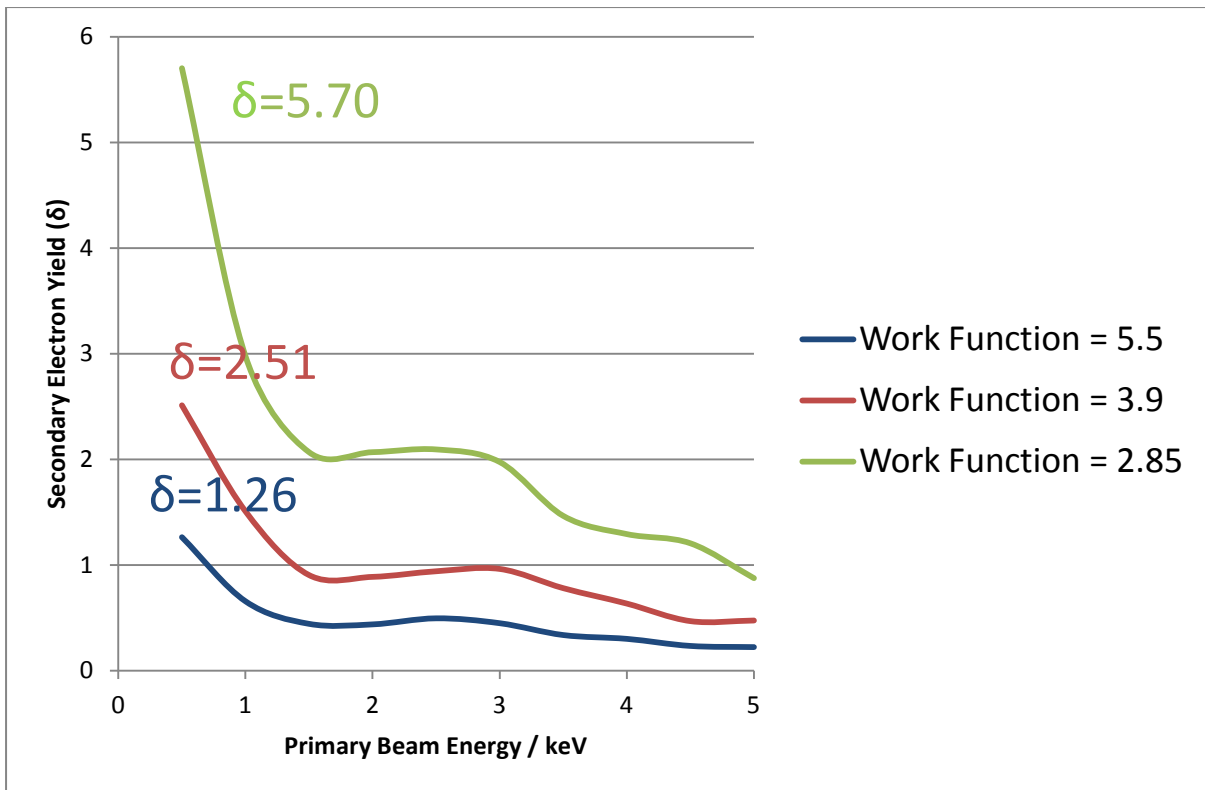


Figure 34: Secondary electron yield curves from simulations of 80 nm thick sample at three different work functions.

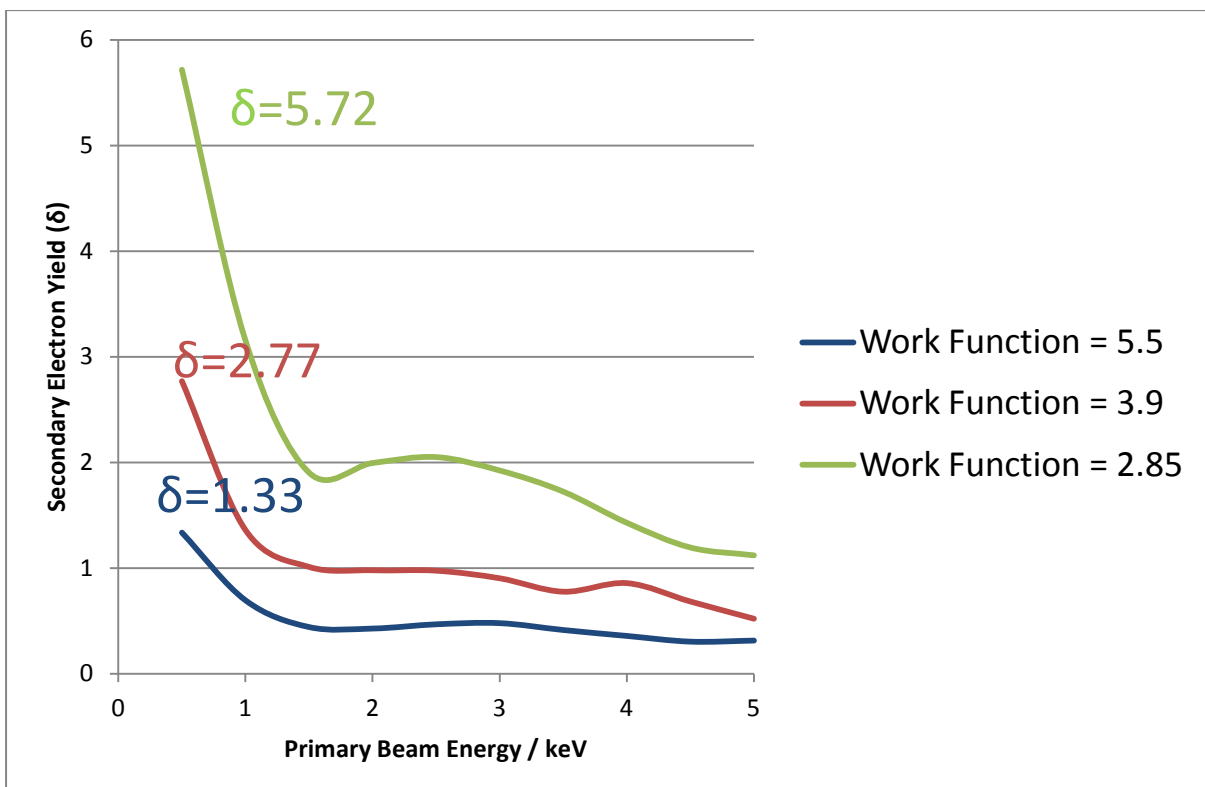


Figure 35: Simulated secondary electron yields curves for 120 nm sample at three work functions.